Influences of depositing materials, processing parameters and heating conditions on material characteristics of laser-cladded hypereutectoid rails

Quan Lai[a,*], Ralph Abrahams[a], Wenyi Yan[a], Cong Qiu[b], Peter Mutton[b], Anna Paradowska[c], Mehdi Soodi[d], Xinhua Wu[e]

[a] Department of Mechanical and Aerospace Engineering, Monash University, Clayton, VIC 3800, Australia
[b] Institute of Railway Technology, Monash University, Clayton, VIC 3800, Australia
[c] Australian Nuclear Science and Technology Organisation, Kirrawee DC, NSW 2232, Australia
[d] Hardchome Engineering, Clayton, VIC 3168, Australia
[e] Department of Materials Science and Engineering, Monash University, Clayton, VIC 3800, Australia

ABSTRACT

The effects of different cladding materials, processing parameters and heating regimes on the underlying microstructural features and mechanical properties of laser-cladded premium rails were investigated by using a hypereutectoid rail grade as a substrate, which is extensively used in heavy-haul rail systems. Cladding materials of 410L, 420SS, Stellite 6 and Stellite 21 with single and double depositions were considered for the comparative study of different cladding materials and processing parameters. To ensure the constant thickness of the claddings for comparison purposes, transverse speed and powder feed rate were modified concurrently in the ranges of 1000–1200 mm/min and 3–4 RPM, respectively. Two heating conditions, i.e. preheating only (HTA) and a combination (HTB) of preheating and post weld heat treatment (PWHT) were applied after the preferable parameters for each cladding material were obtained. The most suitable cladding material for rail-wheel contact was established by assessing all crucial aspects, i.e. surface defects, hardness, microstructural and mechanical properties. Process parameters for each considered cladding material were determined to achieve no surface defects. For cladding layers, application of HTA was not able to significantly modify the microstructures of the deposits, whereas HTB was observed to cause severe cracks in Co-base alloys, i.e. Stellite 6 and Stellite 21. In the heat affected zones (HAZs), irrespective of the cladding materials, the formation of untempered martensite was not avoided by the application of preheating at 350 °C. Consequentially, cracking in the HAZ was observed. An uncracked and desirable microstructure in the HAZs was established using HTB, regardless of the depositing materials. The addition of a second layer did not change the thickness of the HAZs but refined the HAZ's microstructures. Shear punch testing (SPT) and Vickers hardness testing were utilized to characterize mechanical properties for the considered cladding materials and good correlations with the obtained microstructural morphologies were shown.

1. Introduction

Damages, i.e. wear and rolling contact fatigue (RCF), etc., often develop and accumulate at the contact surfaces during the service lives of rail-wheel components, which are commonly the main reasons for preventative maintenance in modern railway infrastructure. The resulting network downtime and expenditure are, therefore, significant. As an encouraging answer, surface treatment of damaged railway components, particularly the laser cladding technique, has been demonstrated its effectiveness.

Laser cladding is a weld build-up process in which a depositing material is adhered to a base material via utilizing a laser. New or damaged engineering components can be metallurgically bonded with superior depositing materials to gain or regain the desired surface properties. Depending on the nature of the applications, different depositing materials can be selected. Recent studies have demonstrated significant improvements in the performance of the laser treated components. Zhenda et al. (1996) conducted an experimental investigation on laser cladding of WC particle-reinforced Ni-based alloy onto AISI 1020 steel. The tribological results indicated the superior wear resistance of the cladded components due to the presence of the claddings. Sexton et al. (2002) performed laser cladding onto aerospace

---

components made of five separate materials and compared to tungsten inert gas (TIG) welding specimens. They indicated that laser cladding offered obvious advantages for the repair of aerospace components and more superior microstructure, hardness, cracking, porosity and dilution levels compared to the TIG specimens. Abioye et al. (2015) laser-cladded austenitic stainless steel AISI 304 components with Inconel 625 wire and reported that an improvement in corrosion performance of the components made of stainless steel was observed due to the protection of the Inconel 625 claddings. These have validated the beneficial impacts on the performance of the treated components by applying laser cladding technology.

Laser cladding is also being tailored to enhance surface properties and corresponding tribological performance of rails and track components while conserving the properties of the parent rail substrate. Many research groups have applied laser surface engineering techniques, i.e. laser glazing and laser cladding, to various rail grades. Aldajah et al. (2003) reported that the use of laser glazing produced a treated rail with a fine and harder solidified microstructure, i.e. as much as three times harder than the substrate. Using similar technique, Shariff et al. (2010) performed laser-glazing on T-12 rail steels, the standard rail grade in India, and reported a marginal reduction in friction coefficient caused by the laser glazed regions. However, the prevention of undesirable plastic deformation, as known as a batter, might be infeasible due to the presence of such high hardness. Niederhauser and Karlsson (2005) investigated the laser cladding treatment of the B 82 steel plates extracted from the Swedish railway wheel with Co-Cr alloys in terms of the cracking and fatigue behaviour. For the cladded steel plates, a consistent and favourable fatigue behaviour was observed. With increasing strain amplitude, an increase in the number of cracks was detected in the plate substrate along with well-plasticized surfaces and shear bands began to connect over grain boundaries were reported on the cladding. Similarly, Ringsberg et al. (2005) studied the RCF behaviour of a Co-Cr alloy layer cladded on the pearlitic UIC 900A (R260) rail steel and reported that excellent agreement between experimental and numerical results of residual stresses was noticed. The behaviour of fatigue failure was strongly influenced by the process of laser cladding compared to the untreated rail. Under the InfraStar project, Franklin et al. (2005) worked on laboratory tests and Hiensch et al. (2005) conducted actual field tests involving RCF and tribological performance of the UIC 900 A rails after being laser cladded. The results from twin-disc laboratory testing showed that the life cycles of the laser cladded specimens were five times greater than that of the base material. Also, the field test results showed no RCF damage. However, the base material in the unclad condition showed clear RCF damage. The research papers have highlighted the importance and significance of utilizing laser cladding in the future rail maintenance strategies. Therefore, understanding and predicting the mechanical performance and metallurgical characteristics of rail steels after cladding are crucial.

However, previous studies have been limited to hypoeutectoid or eutectoid rail grades, and information on the application of laser cladding to premium hypereutectoid rail grades, such as those commonly used in heavy-haul rail systems, is limited in the open literature. These rail grades are renowned for their superior load bearing capacity, better service durability, smaller crack propagation rate and longer maintenance intervals compared to conventional rail grades.

Previous works on laser cladding of hypereutectoid rails by Lai et al. (2017a,b) investigated the effects of cladding direction, heat treatment and carbon dilution on the material properties of a hypereutectoid rail grade using a 410L stainless steel cladding material. The present work focuses on the influence of different cladding materials, processing parameters and heating conditions on microstructural and mechanical characteristics of hypereutectoid rails after cladding. 410L stainless steel, 420SS stainless steel, Stellite 6 and Stellite 21 were selected for the cladding materials. A comparative study of the cladding materials by considering vital aspects, i.e. microstructures, surface defects, hardness, and material strength, was undertaken to determine the preferable cladding material, processing parameters and heating conditions for rail-wheel contact conditions.

To establish functionally graded rails, in this study laser cladding of the cladding materials was applied to 600-mm long sections of premium rail samples utilizing a coaxial fibre laser nozzle. Interpretation of microstructures of both the cladding layers and the HAZ in the rail substrate was achieved based on images of optical microscopy and Scanning Electron Microscopy (SEM). To study and compare the mechanical properties of different depositing materials, shear punch and tensile testing were performed. Indications of wear resistance of cladding layer were obtained via Vickers indentation, thereby, the correlation between the microstructural characteristics and the prediction of wear performance were also established.

2. Experimental procedure

To determine the appropriate cladding materials for wheel-rail contact, four potential materials with appropriate properties, i.e. high wear resistance, great suitability for laser and load bearing capability, etc. were selected, i.e. 410 L (~150 m), 420SS (~150 m), Stellite 6 (45–106 m) and Stellite 21 (45–125 m). Selection of 410L, 420SS, Stellite 6 and Stellite 21 was considered based on their superior surface properties, commercially viability and suitability of surface properties for heavy haul transportation. Clare et al. (2013) and Wang et al. (2014) reported the superior surface properties of these materials, i.e. high strength, excellent wear and corrosion resistance, great laser compatibility and good load carrying capability, which make them suitable for the application to wheel-rail contact. They are commercially available in powder form for laser application, hence the quality of these materials is strictly controlled and accredited by the manufacturers, and they are readily available if the maintenance technique is successfully established. These candidates were centrally cladded onto the head of the rail sections to replicate a typical rail repair. The nominal chemical composition of the chosen cladding materials is listed in Table 1a, and that for the rail material in Table 1b.

Based on the expected requirements for in situ repairs to the rails with the length of 200–800 mm, and to mimic the actual conditions of laser treatment with typical heat sinks and constraints. Selection of 400-mm length and 70-mm width of cladding dimensions was considered to apply on a 600-mm long rail. Such dimensions would allow an extensive investigation at the vital locations of a rail repair, i.e. the starting and ending of the claddings - transient state condition, and the middle sections of claddings – steady state condition. Fig. 1 shows the generic sizes of the laser deposits and substrates of rail steel along with

Table 1a
Chemical composition of the depositing materials.

Materials	Elements (wt.%)															
	Fe	Mn	C	Si	S	P	Ni	Cr	Mo	Cu	V	Nb	Ti	Al	W	Co
410L	Bal	0.51	0.01	0.47	0.01	0.01	0.08	12.7	0.01	0.05	0.01	0.02	< 0.01	0.01		
420SS	Bal	1.17	0.24	0.63	0.01	0.01	0.22	12.6	0.03	0.03	0.02	0.01	< 0.01	0.02		
Stellite 6	0.09	0.02	0.99	1.58	< 0.01	0.03	0.72	28.3	0.01	0.01	< 0.01	< 0.01	0.01	< 0.01	4.10	Bal
Stellite 21	0.16	0.59	0.23	0.86	0.01	0.01	2.28	27.0	5.20	< 0.01	< 0.01	< 0.01	< 0.01	< 0.01	0.05	Bal

Table 1b

Chemical composition of the rail substrate (N.S = Not significant).

Identification	Elements (wt.%)										
	C	Mn	Si	P	S	Cr	Ni	Mo	V	Nb	Al
Rail substrate R400HT [*]	0.93 0.88-1.07	0.95 0.95-1.35	0.28 0.18-0.62	0.018 0.025 (max)	0.014 0.025 (max)	0.20 < 0.30	< 0.01 N.S	< 0.01 N.S	< 0.01 N.S	< 0.01 N.S	< 0.005 0.004

(*) European Committee for Standardization (CEN), EN13674−1:2011 Railway Applications−Track−Rail−Part 1: Vignole railway rails 46kg/m and above.

a defined coordinate system.

Using a laser coaxial nozzle, a 4 kW IPG fibre laser gun was used in conjunction with a powder feeder of Sultzer-Metco twin-10 for the cladding process, in which a melting pool was generated by fusing an alloy addition to the rail substrate. The laser nozzle was monitored and controlled by a 6-axis CNC unit of Motoman XRC SK 16X. The optics were able to precisely establish a circular laser spot with a diameter of 5 mm upon the treated surfaces. To avoid undue oxidation during the laser cladding process, an inert environment was created intentionally around the laser beam by adding a protecting gas - 50% Ar and 50% He. To enhance laser absorptivity and eliminate contaminants, grit-blasting was employed prior to laser treatment.

In the current work, comparative studies of the depositionof the four cladding materials on rail substrate were conducted by changing the heating conditions, process parameters and number of deposited layers. The heating condition of preheating to 350 °C was conducted by using a manual oxy-fuel torch. Three thermocouples were attached to the full rail-head and measured at various cladded regions during the application of preheating to monitor the homogeneity of preheating temperature. Immediately upon the achievement of the preheating temperature of 350 °C across the specimen, laser deposition was initiated. Thereafter, PWHT was carried out to tailor the cooling rate and achieve the desired properties, i.e. microstructure and hardness, for the designed functionally graded material. In addition to the PWHT, ceramic heating blankets were employed to ensure that the temperature of 350 °C across the cross-sections of the specimens was obtained and maintained. Descriptions of the heating conditions used are summarized in Table 2.

To maintain the thickness of the cladding deposits for comparison purposes, laser traversing speed and powder feed rate were modified concurrently and accordingly, while laser power was kept as constant. Transverse speed and powder feed rate were changed in the ranges of 1000–1200 mm/min and 3–4 rpm, respectively. The ranges were selected to give defect-free surface. The process parameter sets are detailed in Table 3. The cladding direction was in the rail-longitudinal direction for all the depositions.

Table 2

Heat treatment procedures applied for the comparative study of heating conditions.

Label	Heat treatment procedures
HTA	Preheating to 350 °C
HTB	Preheating to 350 °C, post-heating to 350 °C and then slow-cooled to room temperature by using a ceramic blanket.

Table 3

Parameter sets and deposited layer number applied for the comparative study.

Specimen Groups	Process parameter sets	No. of deposited layers
G1-1L	1000 mm/min; 3 RPM powder; 3200W	1
G1-2L	1000 mm/min; 3 RPM powder; 3200W	2
G2-1L	1200 mm/min; 4 RPM powder; 3200W	1
G2-2L	1200 mm/min; 4 RPM powder; 3200W	2

Representative metallographic specimens were prepared by sectioning the cladded rails in both rail-transverse and longitudinal directions. The specimens obtained were subjected to standard metallographic specimen preparation, i.e. grinding, mounting, polishing and etching. A two-stage etching procedure was implemented to provide a comprehensive microstructural characterization. In the first stage, Kalling's no. 2 (5 g $CuCl_2$, 100 ml HCl and 100 ml ethanol) and CoM1 (50 ml Distilled water and 50 ml HCl) solutions were used to reveal the microstructure of the stainless steel and Co-base deposits, respectively. A 2% Nital etchant was used in the second stage to study the rail steel substrate's microstructure. An optical microscope - Nikon Eclipse and a scanning electron microscope - JEOL 7001 F FEG were utilized to perform the microstructural characterization of the specimens. Evaluation of the mechanical properties of the cladded layers was achieved via the
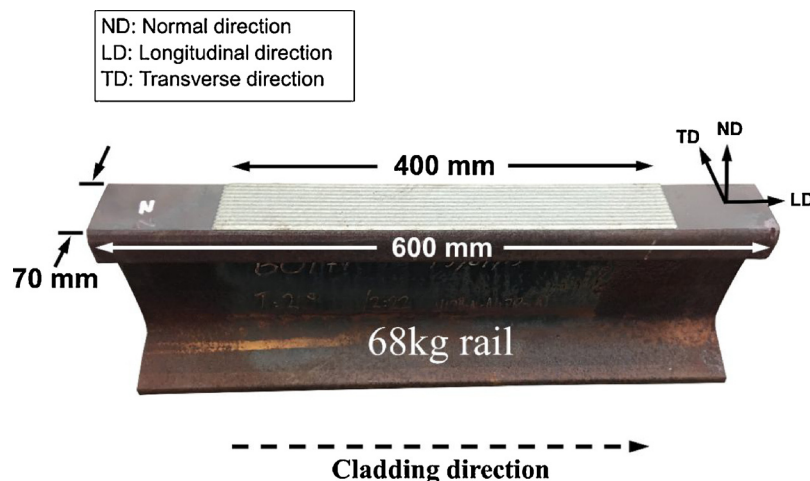

Fig. 1. Photograph of a laser-cladded hypereutectoid rail specimen with detailed dimensions prior to specimen preparation process.
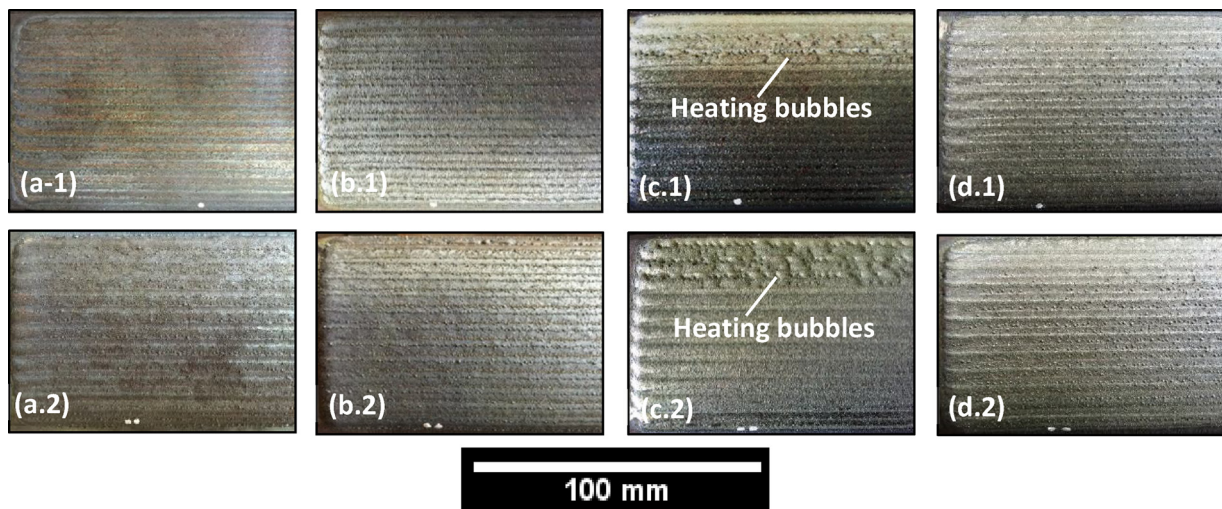
Fig. 2. Micrographs of representative top surfaces of Group 1 deposits with (1) single and (2) double layer cladding passes. Heat treatment produces involved only preheating to 350 ℃ (HTA). (a) 410 L, (b) 420SS, (c) Stellite 6 and (d) Stellite 21.

Struers A300 Duramin hardness tester and shear punch tests. Shear punch specimens were prepared using Electrical Discharge Machining (EDM). The shear punch tests were conducted with a 1.5 mm diameter punch on the EDM slices of 2 mm thicknesses, which were extracted from the claddings of all the considered cladding materials.

3. Results

3.1. Comparative studies of suitable processing parameters and heat treatments

To obtain defect-free surfaces and identify the appropriate process parameters and heat treatments, an investigation of surface defects and structural integrity of the cladded rails using the studied cladding materials was conducted. High-quality close-up images of the top surfaces for each of the specimen groups are shown in the following figures. For Group 1 with only preheating (HTA), except for Stellite 6 deposits, all other single deposition showed intact cladding surfaces with no visible surface cracks, as shown in Fig. 2(a.1)–(d.1). Stellite 6 deposits were found to have surface bubbles, as shown in Fig. 2(c.1). The molten pool evaporated and voids formed towards the last laser tracks. For double deposition, similar characteristics were found, as shown in Fig. 2(a.2)–(d.2), but the surface bubbles were more severe for Stellite 6, as shown in Fig. 2(c.2).

With an increase in the transverse speed and powder feed rate yet constant cladding thickness, cladding surfaces subjected to HTA for Group 2 single and double depositions were found to be free of surface defects as shown in Fig. 3(a.1)–(d.1) and (a.2)–(d.2), respectively. However, for 410L stainless steel, the second deposition with the traverse speed of 1200 mm/min and 4 RPM was found to cause the molten stainless steel to evaporate, as shown in Fig. 3(a.2).

In summary, regardless of the number of clad layers, a defect-free surface of the 410 L clads was achieved by using Group 1 processing parameters, as shown in Fig. 2–4(a.1) and (a.2). It implies that the upper limit of laser traverse speed for the 410 L cladding materials is 1200 mm/min (Group 2). Otherwise, heating problems associated with the evaporation of the cladding materials will occur.

The surface integrity for Stellite 6 cladding is affected by the traverse speed of the laser source. At 1000 mm/min (Group 1) of traverse speed, both Stellite 6 clads with one and two layers exhibited heating bubbles at the last laser tracks as shown in Fig. 2(c.1) and (c.2). Whereas for the cladding processed at 1200 mm/min (Group 2) with no heating problems were observed, as shown in Fig. 3 (c.1) and (c.2). It suggests that the lower limit of traverse speed for Stellite 6 is 1000 mm/

min. Finally, for 420SS and Stellite 21, surfaces of the claddings processed at 1000 mm/min and 1200 mm/min were free of bubbling problems.

To control the hardness of the claddings and their corresponding HAZs, HTB was employed for the specimen groups observed with no defects and good surface integrity. Group 1 (1000 mm/min; 3 RPM powder and 3200 W) was chosen to apply HTB for 410 L stainless steel as shown in Fig. 4(a.1)–(a.2), whereas Group 2 (1200 mm/min; 4 RPM powder; 3200 W) was selected to apply HTB for 420SS, Stellite 6 and Stellite 21 as shown in Fig. 4(b.1)–(b.2), (c.1)–(c.2) and (d.1)–(d.2). By repeating these parameters, the specimens obtained showed similar morphologies, i.e. no voids nor bubbling problems, compared with those subjected to HTA as shown in Fig. 4.

3.2. Microstructural characteristics of the four deposited layers

Based on the above results, the cladded rails with defect-free surfaces were subjected to further microstructural analyses. Typical cross sections for the four comparative specimen groups of 410L, 420SS, Stellite 6 and Stellite 21 are shown in Fig. 5–8, respectively. Each of these figures shows four separate micrographs which refer to a different number of cladding layers and the applied heat treatments.

The 410 L single-layer deposits subjected to HTA and HTB were observed with similar microstructural characteristics regarding metallurgical phases, as shown in Fig. 5(a) and (c), respectively. Lai et al. (2017b) investigated the effects of altering cladding directions on the microstructural and mechanical characteristics of rails cladded with 410L and reported colonies of ferrite inside a martensitic matrix. In the current investigation, comparable microstructural characteristics were found in the 410L deposits. Regardless of the heat treatments applied, ferritic grains dominate the regions near the top surface of the claddings and the overlapping regions of one track and the subsequent track, as shown in Fig. 9(i) and (ii). For double layers, the ferritic grains formed in the first deposition were joint with those of the latter deposition. Hence, the nucleation site of ferritic grains was close to the fusion line between the two layers. Large grains of ferrite were observed to elongate through the thickness of the second layer due to the absence of preheating temperature. The main microstructures of the second layer consist of large ferritic dendrites and a small portion of martensite as shown in Fig. 5(b) and (d). Whereas martensite was the main microstructure of the first layer, regardless of the heat treatments applied, as shown in Fig. 9 (iii) and (iv).

The overview micrographs of 420SS deposits with single deposition showed a significant portion of fine martensitic dendrites, as shown in
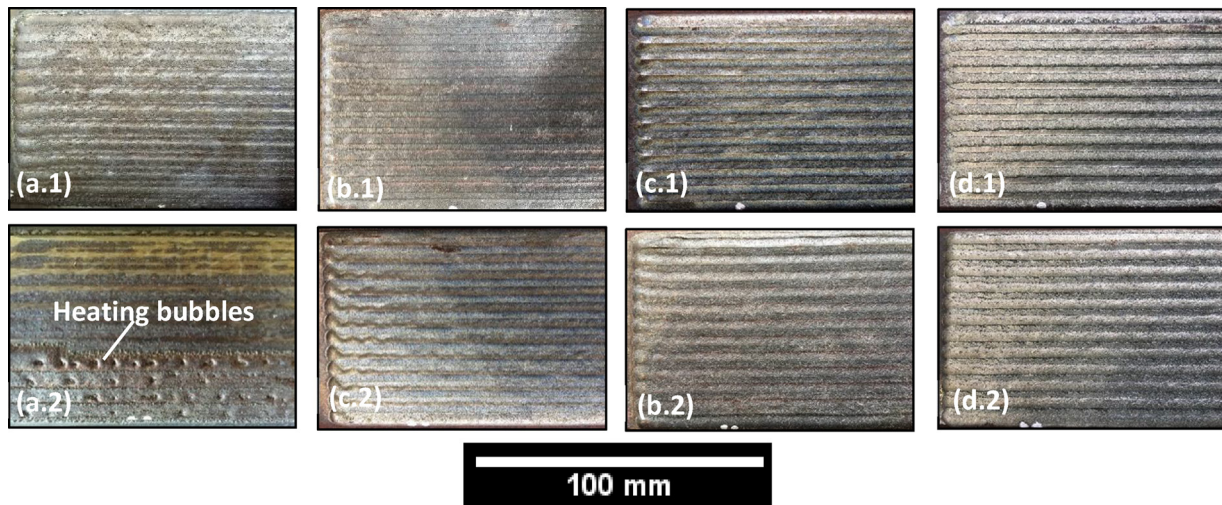
Fig. 3. Micrographs of representative top surfaces of Group 2 deposits with (1) single and (2) double layer cladding passes. Heat treatment produces involved only preheating to 350 ℃ (HTA). (a) 410 L, (b) 420SS, (c) Stellite 6 and (d) Stellite 21.

Fig. 6(a) and (c). Previous works by Hemmati et al. (2011) and Kou (2003) collectively showed the influences of two factors, i.e. the temperature gradient and the growth rate of solid-liquid interface, on the microstructural characteristics of the cladding deposits. The factors varied inversely from each other as moving through the cladding's thickness, and hence, three resulting dendritic morphologies were detected, i.e. Equiaxed, Columnar/cellular and Planar dendrites, irrespective of the heat treatments applied. Similar microstructural characteristics were observed in the 420SS deposits with double deposition, as shown in Fig. 6(b) and (d). Fig. 10(i)–(iv) show micrographs of typical microstructural characteristics of the 420SS deposits at higher magnifications.

Fig. 7(a) and (b) showed micrographs of single and double layer Stellite 6 deposits which was subjected to HTA, respectively. An investigation by Farnia et al. (2012) reported that Co-rich dendrites enclosed by regions of interdendritic lamellar with W, Cr and Co carbides were observed for the microstructures of Stellite 6. In the current work, microstructural characteristics of the Stellite 6 deposits were observed to be consistent with those of the previous work through the thickness of the deposits. Typical dendritic morphologies were observed and shown in Fig. 11(i)–(iv), and no significant variations in microstructural characteristics were detected between the laser track's overlap, and

other cladding regions were detected. For the Stellite 6 deposits subjected to HTB, microstructures with similar characteristics to those of HTA were observed. Nevertheless, cracks were observed to occur in subsurface regions of the deposits for both single and double layers, particularly at the overlapping or remelted regions of the cladding tracks, as shown in Fig. 7 (c) and (d). The carbide grain boundaries where ductility was reduced by the formation of the hard and brittle carbides were observed to be sites for crack propagation, as shown in Fig. 11(v) and (vi). Brandt et al. (2009) reported that the presence of intergranular cracks might be attributed to the combined effects of several factors, i.e. dilution from the hypereutectoid rail substrate, excessive cladding temperature, creep deformation required for relaxation of the residual stresses owing to the application of PWHT, etc. Cracking of the Stellite 6 deposits as subjected to HTB was observed with similar characteristics to the PWHT cracking phenomenon, commonly occurred in the low alloy steels containing additions of Cr, Mo and Co, and subjected to PWHT, which might adversely influence the application of the deposits.

For Stellite 21, optical micrographs of the cross sections of single and double layer specimens subjected to HTA, as shown in Fig. 8(a) and (b) respectively, showed microstructures including Co-rich primary dendrites and interdendritic regions with hard carbides, as shown in
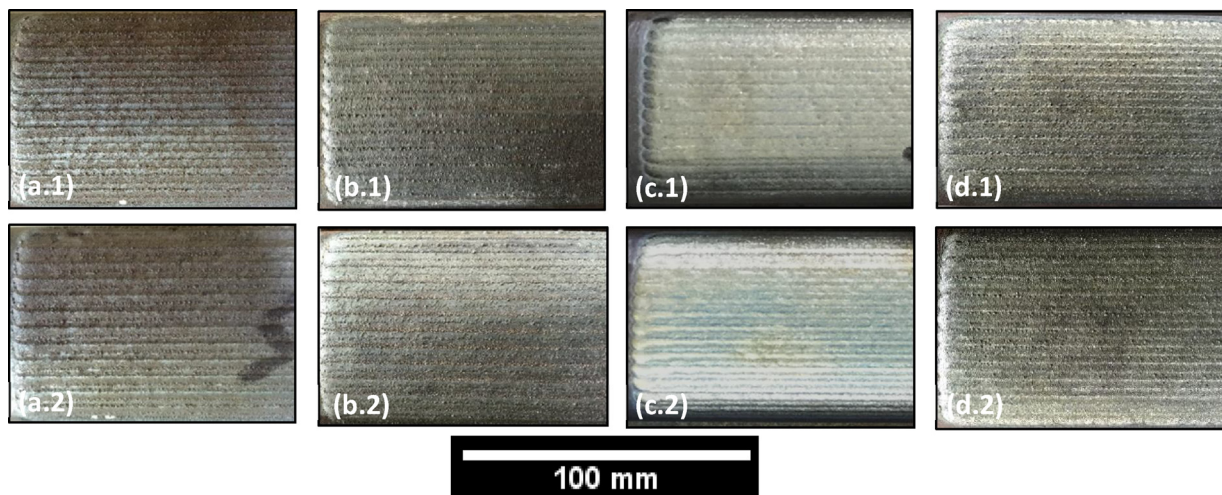

Fig. 4. Micrographs of representative top surfaces of the deposits with the desired surface properties. Heat treatment produces involved preheating to 350 ℃, post-heating to 350 ℃ and then was slow-cooled to room temperature by using ceramic blanket (HTB). (a) 410 L - Group 1, (b) 420SS - Group 2, (c) Stellite 6 - Group 2 and (d) Stellite 21 - Group 2 with (1) single and (2) double layer cladding passes.
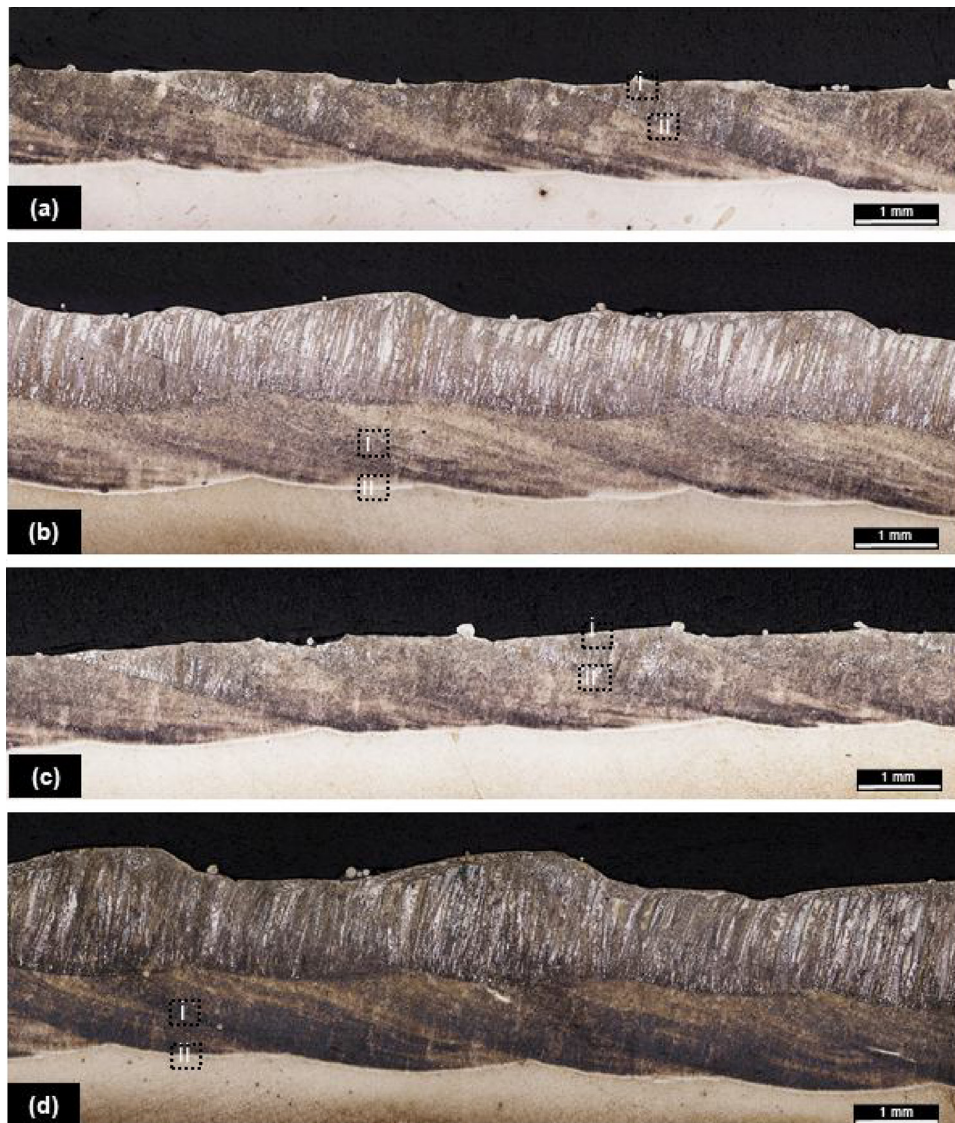
Fig. 5. Micrographs showing typical cross sections of 410 L deposits with (a) single deposition and HTA, (b) double deposition and HTA, (c) single deposition and HTB, and (d) double deposition and HTB.

Fig. 12(i)–(iv). Investigation of Rajeev et al. (2017) reported that, due to the nature of Stellite 21's elements, microstructures of Stellite 21 contained a complex set of carbides in a Cr-Co-Mo matrix. Nevertheless, cracks occurred periodically in the remelted/overlapping regions of the Stellite 6 deposits subjected to HTB, and the cladding-substrate interface was the preferred site for crack initiation, as shown in Fig. 8(c) and (d). Magnified micrographs of cracking of Stellite 21 deposits subjected to HTB are shown in Fig. 12(v) and (vi). Addition of a second cladding layer was observed to increase the crack length. It might be attributed to the alloying elements of W, Cr and Mo in Stellite 21, and reheating/remelting during multi-track cladding. In other words, the remelted/overlapping regions of one laser track would be considered as the heat affected zones of the subsequent laser tracks.

3.3. Influence of heat treatment and cladding materials on microstructures of the HAZs

Optical macrographs of cladded rails in the transverse direction were obtained to investigate and compare the microstructural characteristics of the HAZs of the four studied cladding materials. Similar to a previous investigation performed by Lai et al. (2017b), the establishment of numerous HAZ sub-regions was detected as a result of the

rail's microstructure subjected to the thermal impacts of the laser cladding treatment. Irrespective of the depositing materials, four typical sub-regions, i.e. i) Partially molten, ii) Coarse-grained, iii) Fine-grained, iv) Spheroidised/partial spheroidised HAZ, were detected.

As shown in Fig. 3(a), the typical microstructure of the coarse-grained regions was characterized by bainitic morphology, whereas the fine-grained regions were characterized with bainitic and pearlitic morphology. Spheroidised/partial spheroidised microstructure was found to locate contiguous to the unaffected substrate, as shown in Fig. 13(b).

Due to the amount of information and similarity of the microstructural evolution in the HAZ subregions of different laser cladded rails samples, which were already published in the previous investigation performed by (Lai et al., 2017a,b), only the different microstructures of the subregions of the HAZ obtained in this current study were labelled in the macrostructure images given in Figs. 14 and 15. Therefore, the macrostructure images - Figs. 14 and 15, were used only to map the effects of the heating conditions and cladding materials on the microstructural characteristics of the HAZ, particularly the martensitic formation.
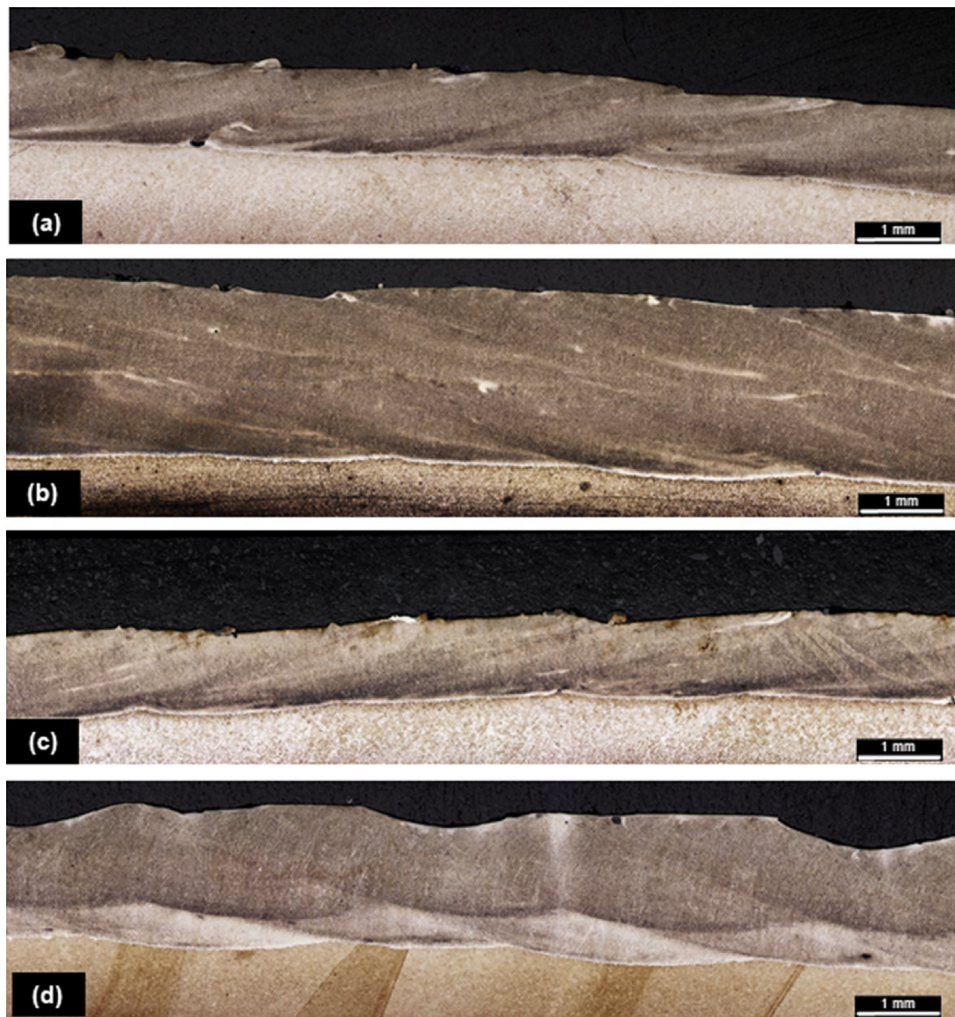
Fig. 6. Micrographs showing typical cross sections of 420SS deposits with (a) single deposition and HTA, (b) double deposition and HTA, (c) single deposition and HTB, and (d) double deposition and HTB.

3.3.1. Microstructural properties of the HAZ with a single deposition

For single deposition treated with HTA, the optical macrographs of the four materials, i.e. (i) 410 L, (ii) 420SS, (iii) Stellite 6 and (iv) Stellite 21 undergone HTA and subjected to single as are shown in Fig. 14. For each material, the four individual macrographs correspond to (a) the initial cladding runs, (b) the middle cladding runs, (c) the last cladding runs, and (d) typical longitudinal sections at the beginning and finishing ends of the cladding runs. Likewise, specimens subjected to HTB with single deposition were also found with the preceding microstructural characteristics in the HAZs, as shown in Fig. 15.

However, owing to the difference in the melting point of the cladding powders, effects of the preheating conditions on the microstructural characteristics of the HAZ of the cladded rails is dependent on the cladding materials. As a result, a martensitic morphology dominated the coarse-grained HAZ at (c) the last cladding runs, and (d) the starting and finishing cladding ends, as shown in Fig. 15. For 420SS and Stellite 6, martensite was observed even in the fine-grained HAZ and spheroidised/partial spheroidised zone as shown in Fig. 14(ii)(d) and Fig. 14(iii)(d). Due to the brittle nature of martensitic phase, cracking was found in the HAZ as evident in Fig. 14(iii)(d).

In single layer deposition subjected to HTB, the addition of PWHT and slow cooling altered the characteristics of microstructure and morphology of the HAZs. Martensite was mitigated in volumetric extent and tempered by reducing the cooling rate and maintaining the heating temperature below the eutectoid temperature for a long period, respectively. The dominance of martensitic phase at (c) the last cladding

runs, and (d) the starting and finishing cladding ends was eliminated and replaced with tempered martensite as shown in Fig. 15(i)(d) and (ii)(d), or even bainitic morphology as shown in Fig. 15(iii)(d) and (iv) (d). No cracking was discerned in Fig. 15.

The achieved results collectively suggested that the application of HTA was, by itself, incapable of preventing the martensitic transformation in the HAZ for all cladding materials listed in Table 1a, particularly at the RHS sections, as shown in Fig. 14(c). No martensitic transformation was found at the LHS sections and the middle sections, as shown in Fig. 14(a) and (b) respectively. It may be attributed to the reduction in the temperature of preheating over time at the RHS sections, as a result of the moving pattern of the heat source between gauge corners. Therefore, the effectiveness of the applied preheating on preventing the occurence of quenching phenomenon at the RHS sections was adversely affected. Using SEM, the other typical features of the microstructure of the LHS sections were observed to be bainitic and pearlitic morphology. The microstructure of HAZs in the longitudinal section was found with martensite, which was consistent with those in the transverse sections. It can be inferred that the preheating temperature of 350 °C at 400-mm length of depositing was inadequate to prevent martensite from forming in the HAZ. Martensitic microstructures are known to result in lower toughness and greater cracking potential. Cracking was, therefore, detected in the HAZ, where martensite as evident in Fig. 14(iii)(d).

The functions of PWHT in Group 2 specimens were to mitigate the residual stresses introduced by the cladding process, tailor the hardness
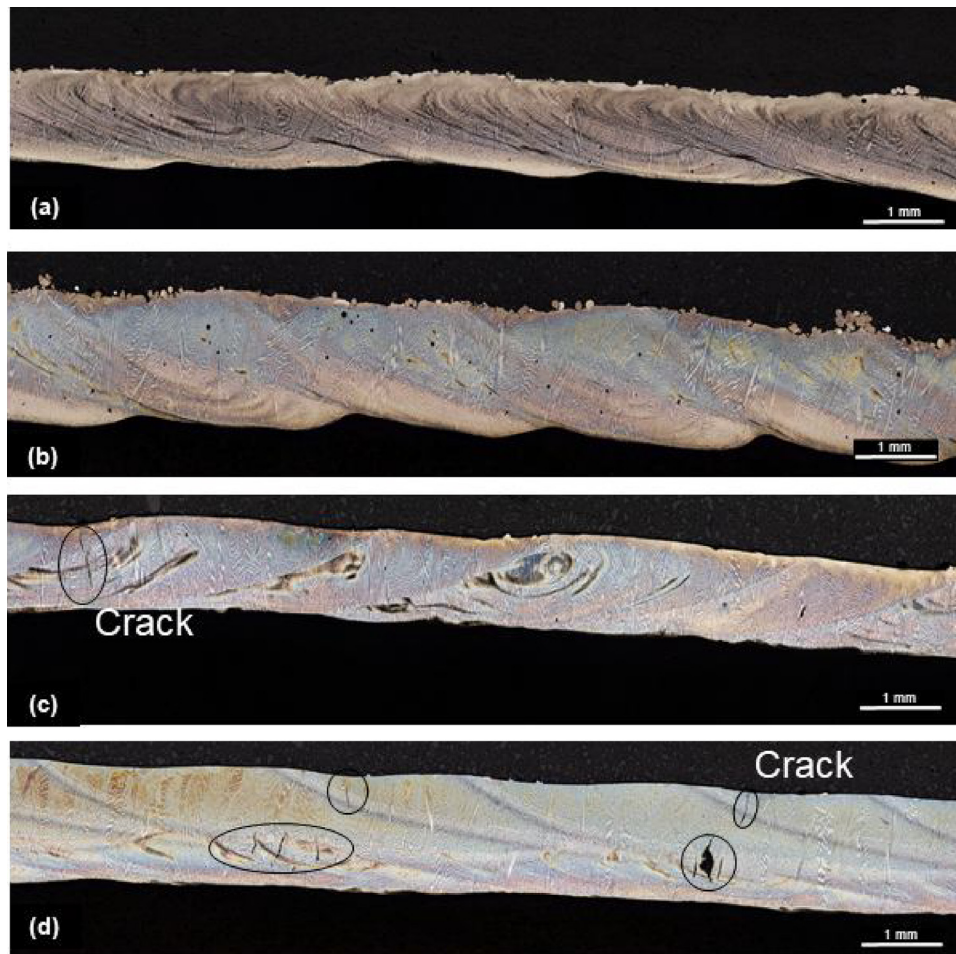
Fig. 7. Micrographs showing typical cross sections of Stellite 6 deposits with (a) single deposition and HTA, (b) double deposition and HTA, (c) single deposition and HTB, and (d) double deposition and HTB.

values of the claddings, and improve the material properties of the claddings. Substitution of tempered martensitic morphology was achieved, particularly at the ends of the laser runs, hence cracking was able to be controlled by the tempering effects of PWHT. It also indicates the minimal effects of using PWHT on avoiding martensitic formation in the HAZ. However, this is based on the observation of one sample; assessment of more samples is required to fully establish the effect of PWHT on the reduction of residual stress levels and the tendency to avoid crack formation.

3.3.2. Microstructural properties of the HAZ with double deposition

Macrographs of the four cladding materials are shown in Figs. 16 and 17 to map the effects of the heating conditions and cladding materials on the microstructural characteristics of the HAZ. Similar microstructural characteristics to the single deposition were observed in the HAZ of the laser cladded rails with double deposition. The microstructural characteristics in the four sub-regions of the HAZ were consistent for all cladding materials as shown in the macrographs - Figs. 16 and 17. Martensite was discernible for the groups of specimens subjected to HTA, particularly at (c) the last laser tracks, and (d) the starting and finishing track ends, as shown in Fig. 16, due to the rapid heat dissipation caused by the thermal sinking effect of bulk rail substrate.

Due to the application of PWHT in HTB, tempered martensite developed in the HAZs of the cladded rails, as shown in Fig. 17. Additionally, the sub-regions, i.e. fine-grained and spheroidised/partial spheroidised regions, were found to develop twice in two separate regions across the HAZ's thickness. It was attributed to the overlapping of

HAZs in the multiple layer deposition.

By depositing layer by layer to build-up thickness of the deposits, the heat absorbed in melting the previous deposit caused less heat penetration into the substrate. Therefore, HAZs of the second layers appeared thinner and in the middle of the previous HAZ. The heat produced by the second deposition did not avoid the formation of martensite in the HAZs by being distant from the HAZ, thus not prolonging the cooling rate of the HAZ, and in fact, may increase the probability of it occurring.

The resulting peak temperature of the HAZ in the second deposition may be lower than that of the first deposition due to the long distance between the heat source and the HAZs of the second layers. Additionally, the thermal gradient was more significant in the second deposition because of the drop in the effective temperature of preheating over time via thermal convection and conduction. Thus quenching phenomenon was more likely to occur. As a result, martensite was found almost across the entire HAZ of second layers as evident in Figs. 16 and 17.

With the aid of an image analysing software, thickness measurements of HAZs of the four depositing materials subjected to HTA (preheating only) and HTB (preheating, PWHT and slow cooling) were determined and correlated to the aforementioned microstructural characteristics, as shown in Fig. 18.

For most of the depositing materials, the variation in HAZ's thicknesses between single and double deposition was not significant. It may suggest that the thickness of HAZs is likely to be independent on the number of deposited layers but strongly depends on the first deposition.

PWHT did not determine the size and volume of the HAZs obtained
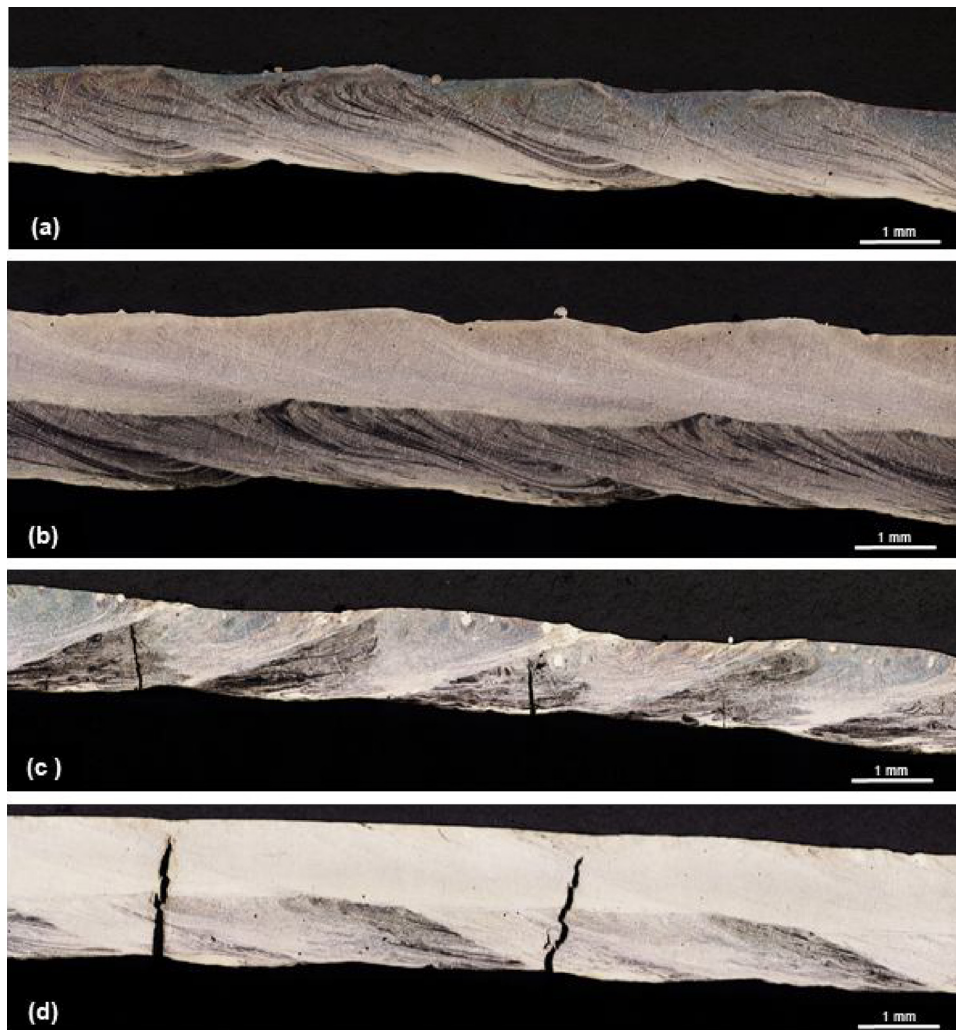
Fig. 8. Micrographs showing typical cross sections of Stellite 21 deposits with (a) single deposition and HTA, (b) double deposition and HTA, (c) single deposition and HTB, and (d) double deposition and HTB.

due to the fact that laser cladding involves a rapid solidification process. However, variations of few hundred micrometres in thickness between HAZs undergone HTA and HTB were detected. It is possible that there may be some processing discrepancies such as the mis-alignment of the laser beam and powder focus, and wearing of the powder nozzle which led to the loss of depositing materials.

3.4. Microhardness tests

A 5 kgf Vickers indentation was used to investigate the influence of changing depositing materials and heat treatments on the hardness of laser cladded hypereutectoid rails. Measurements were performed on the rail-transverse sections, i.e. middle, right and left gauge corner sections, of the four depositing materials subjected to two different heat treatment regimes.

The vertical microhardness distribution of 410L is shown in Fig. 19(a). The 410L cladding layers, subjected to HTA, were de-termined with average hardness values of 372 HV and 375 HV for single and double deposition, respectively. As subjected to HTB, the average hardness values of cladding were 356 HV and 362 HV for single and double deposition, respectively. For the HAZs, the average hardness values were determined to be 457 HV and 490HV respectively for single and double deposition undergone HTA, whereas, specimens which were subjected to HTB, the average hardness values of HAZ were measured to be 385 HV and 356 HV respectively for single and double deposition.

For 420SS, the vertical microhardness variation of the cross sections subjected to HTA is shown in Fig. 20(b). Average hardness values of 649 HV and 629 HV were obtained respectively for the claddings with single and double deposition. The average hardness values of the cor-responding HAZs were 457 HV and 490 HV. Under HTB, average hardness values of the claddings for single and double deposition were determined respectively to be 572 HV and 531 HV, while their corre-sponding average hardness values of HAZ were 417 HV and 347 HV, respectively.

Average hardness values were 441 HV and 501 HV for the cross sections under HTA of Stellite 6 deposits with single and double layers respectively, as shown in Fig. 19(c). The corresponding average hard-ness values of the HAZ were found to be 368 HV and 334 HV. For the single and double layer specimens treated with HTB, the average hardness values of the deposits were 452 HV and 441 HV, and the average hardness values of the HAZ were 395 HV and 359 HV, re-spectively.

Vertical microhardness distribution of the Stellite 21 cladded rails is shown in Fig. 19(d). Average hardness values of 390 HV and 420 HV were achieved for the single and double layer deposits subjected to HTA. Whereas, the corresponding HAZ's average hardness values were 379 HV and 339 HV. For specimens treated with HTB, the average hardness values of the single and double depositions were decreased to 362 HV and 337 HV respectively, and 361 HV and 336 HV for the cor-responding HAZs of the single and double depositions.
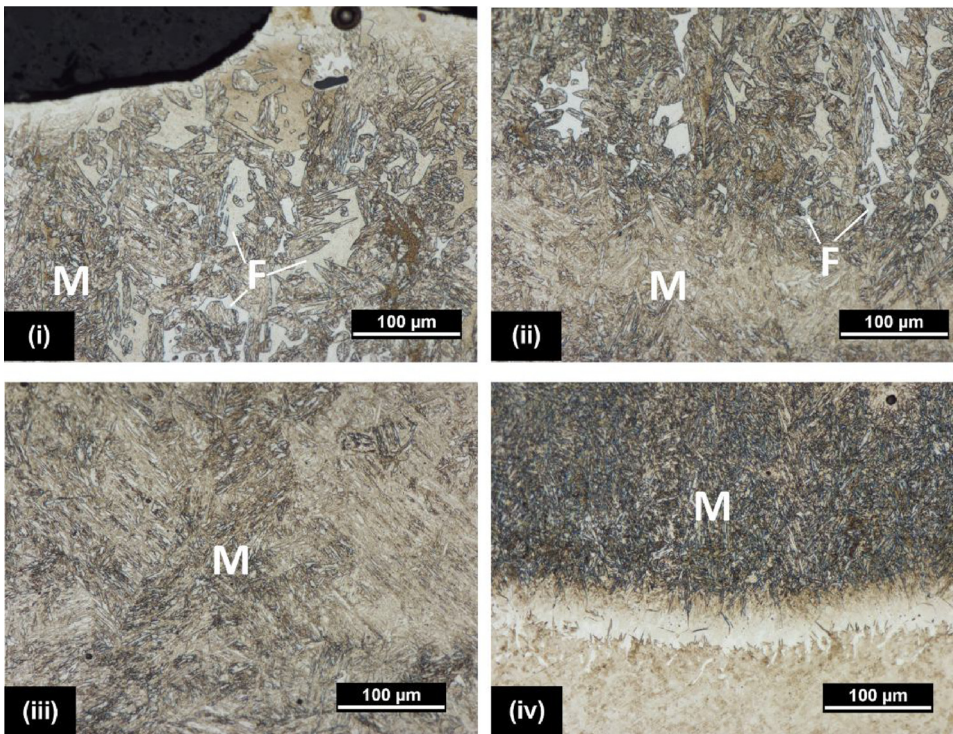
Fig. 9. Representative micrographs of cross sections of 410 L deposits with single deposition, (i) top region of laser tracks (ii) overlapping region of laser tracks, whose locations are shown in Fig. 6(a) and (b). For double deposition, representative micrographs of the first layer, (iii) middle region of laser tracks, and (iv) interface of deposit-substrate, whose locations are shown in Fig. 6(c) and (d).
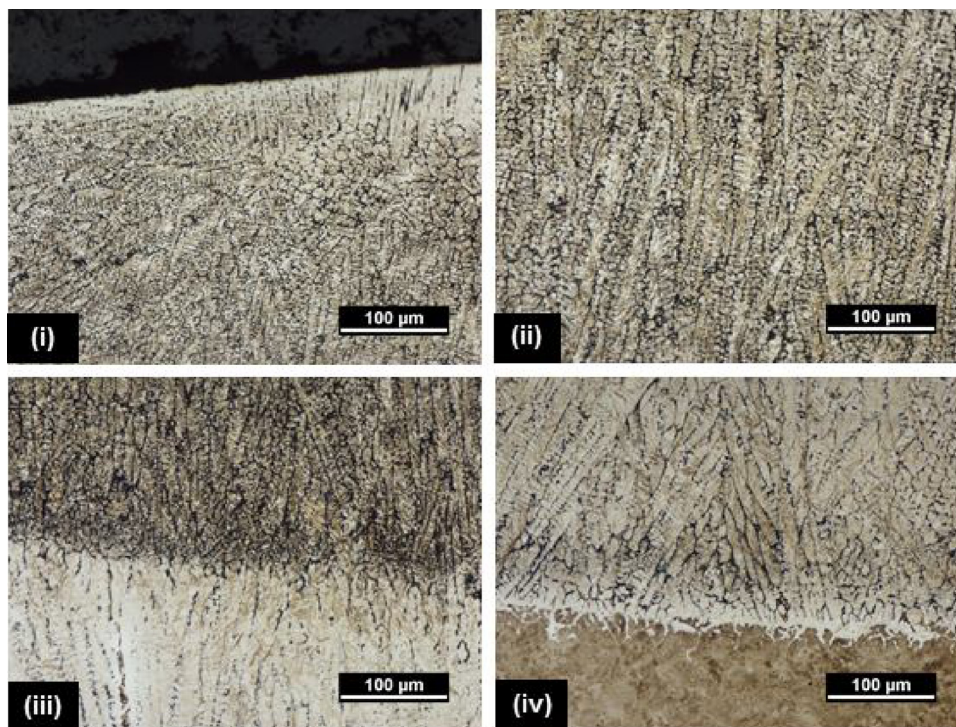

Fig. 10. Representative micrographs of cross sections of 420SS deposits, regardless of the heat treatment applied and number of layers, (i) top region of laser tracks (ii) overlapping region of laser tracks, (iii) interface of deposits for double deposition, and (iv) interface of deposit-substrate, whose locations are shown in Fig. 7.

Regardless of the cladding materials and the number of layers, minor decreases in the average hardness were observed in the cladding layers and the corresponding HAZs treated with HTB compared to those subjected to HTA. It might be attributed to the application of PWHT, which tempered the microstructures. The reduction in hardness was necessary to comply with the hardness requirements of between 400 and 500 HV and to temper any martensite formed in the HAZ, hence reducing the tendency of cracking. Investigations by Harati et al.

(2014); Xu et al. (2006) and Ganesh et al. (2010) reported that, during the process of double deposition of Co-base alloys, remelting or re-heating occurred and affected the microstructure of the first layer. Hardness values of the first layers were, therefore, lower than those of the second layers.

In the current work, effects of depositing multi-layers on hardness distribution were also observed in the deposits of Co-base alloys, i.e. Stellite 6 and Stellite 21, but not obvious in the stainless-steel deposits,
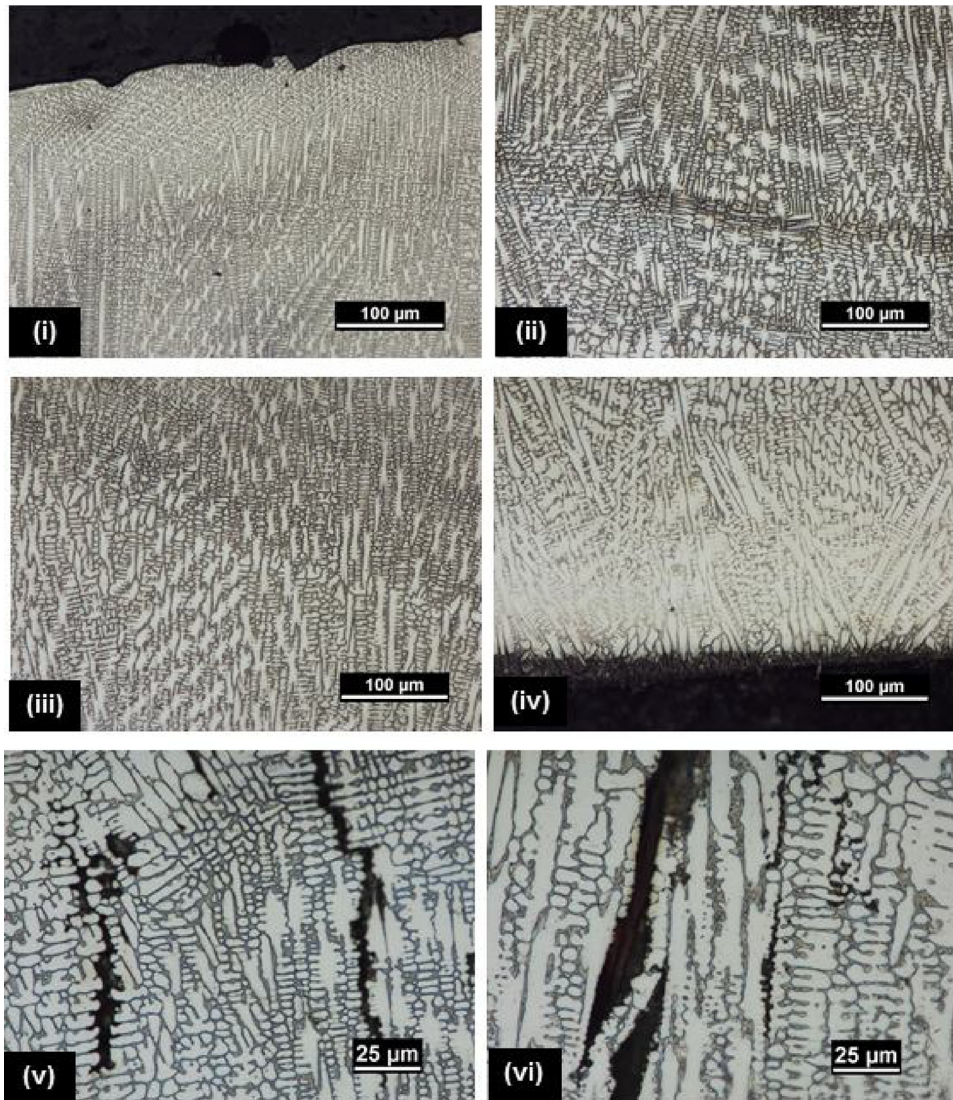
Fig. 11. Representative micrographs of cross sections of Stellite 6 deposits subjected to HTA and with single deposition, (i) top region of laser tracks (ii) overlapping region of laser tracks, (iii) middle region of laser tracks, and (iv) interface of deposit-substrate, whose locations are shown in Fig. 8. (v) & (vi) Magnified micrographs of cracking of Stellite 6 deposits subjected to HTB at different locations.

i.e. 410 L and 420SS, as shown in Fig. 19. Similar to the previous investigations by Lai et al. (2017b), the hardness distribution of the 410 L deposits showed high hardness values from the cladding-substrate interface to the fusion line between the two deposits (x ≈ 1 mm), as shown in Fig. 19(a), due to the carbon dilution from the substrate of hypereutectoid rail to the deposits.

As a result of the high carbon content in the composition of 420SS, as shown in Table 1a, high hardness values associated with the microstructure of 420SS were detected for the specimens under preheating only (HTA) as shown in Figs. 6 & 10. Depending on the amount of heat input into the 420SS workpieces, a reduction in hardness of the 420SS deposits might be varied. In Fig. 19(b), the single deposition treated with HTA had the least amount of heat input. Hence, the corresponding average hardness reached the highest value of 649 HV as shown in 420SS-1L-HTA. In adding more cladding layers, the average hardness values of cladding were reduced due to the increase in heat input, i.e. double deposition with HTA - 629 HV, as shown in 420SS-2L-HTA. Similarly, hardness value of single deposition undergone HTB, as shown in 420SS-1L-HTB, is lower than that of double deposition undergone HTB, as shown in 420SS-2L-HTB. When being treated with HTB, the addition of PWHT inputs more heat than those with HTA, which also allows tempering of the martensitic microstructure. As a result, single

deposition and double deposition claddings which were subjected to HTB were respectively given lower hardness of 572 HV and 531 HV which are lower than those with HTA for the same processing parameters.

3.5. Evaluation of the shear strength of the laser cladded rails

Johnson (1987) reported the development of shear stress under wheel-rail contact, which is one of the vital causes of railway damage. Locations with high shear stresses are commonly observed with rolling contact fatigue (RCF) defects. Traction/adhesion and creepage are influencing parameters which decide such locations. Conditions with low creepage are established with T/N < 0.3 at the contact patch, where T and N are respectively the tangential and normal forces, and consequently the maximum shear stress occurs at subsurface levels. On the other hand, T/N > 0.3 is associated with high creepage conditions, where shear stress is detected to be maximum at the surface. Furthermore, Magel (2011) reported that material behaviour, i.e. RCF damage and cumulative wear, was found to be governed by the magnitude and the locations of the local stresses.

Therefore, the shear strength of the cladded rails ought to be determined and compared to that of virgin rails. By successfully obtaining
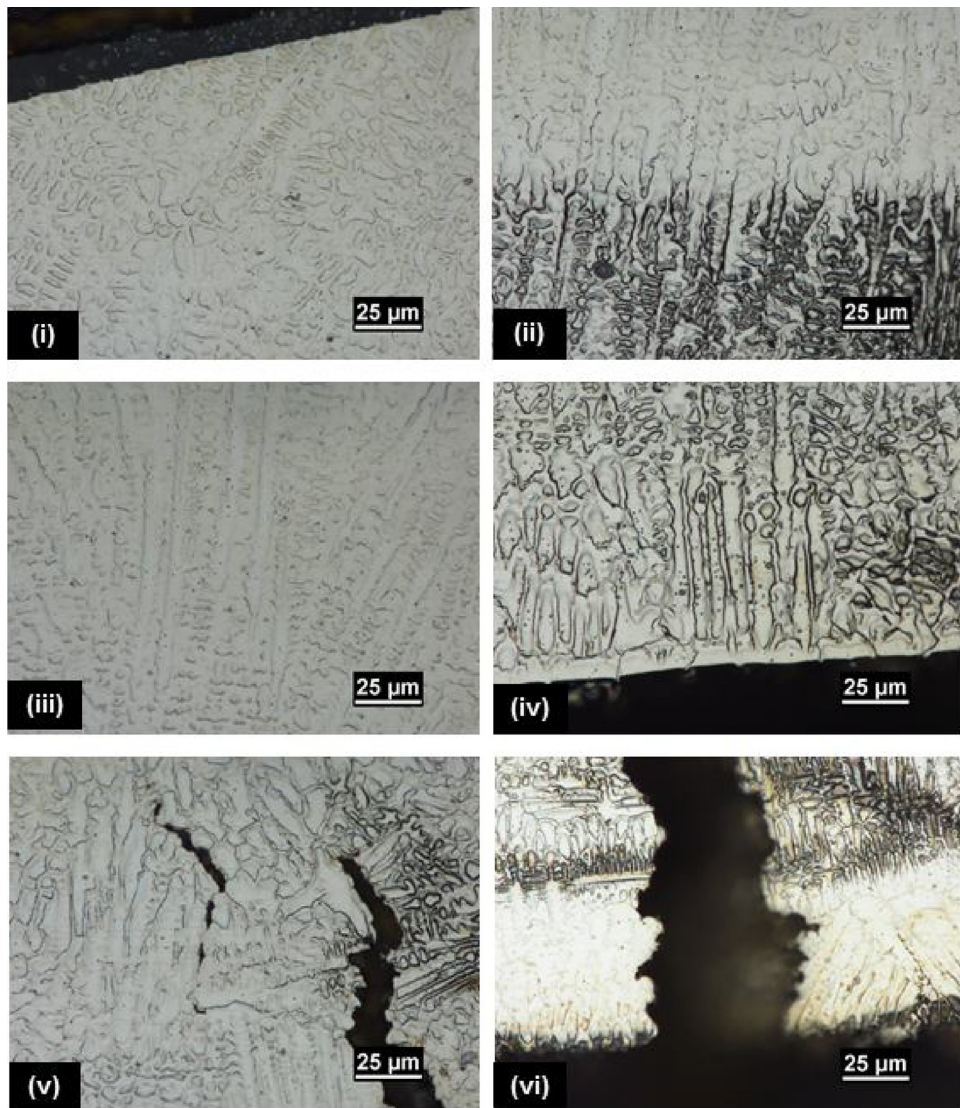
Fig. 12. Representative micrographs of cross sections of Stellite 21 deposits subjected to HTA and with single deposition, (i) top region of laser tracks (ii) overlapping region of laser tracks, (iii) middle region of laser tracks, and (iv) interface of deposit-substrate, whose locations are shown in Fig. 9. (v) & (vi) Magnified micrographs of cracking of Stellite 21 deposits subjected to HTB.

the mechanical properties, i.e. shear strength, ultimate shear strength, tensile yield strength, ultimate tensile strength, etc. from shear punch tests, Guduru et al. (2005) and Hankin et al. (2000) have established a useful tool to evaluate the material behaviour of small-sized specimens. In the current investigation, shear punch testing was selected to perform on the cladded rail, given that the cladding thickness was thin.

To establish a reference stiffness curve, a sample of 0.6 mm thickness was prepared from the parent rail material which complied with the specified the requirements outlined in EN 13674-1 (2011) for the R400HT grade. Fig. 20 shows the average plots of five results for every tested specimen. The pearlitic rail steel sample failed at a shearing force of 5380 N and the corresponding ultimate shear strength of
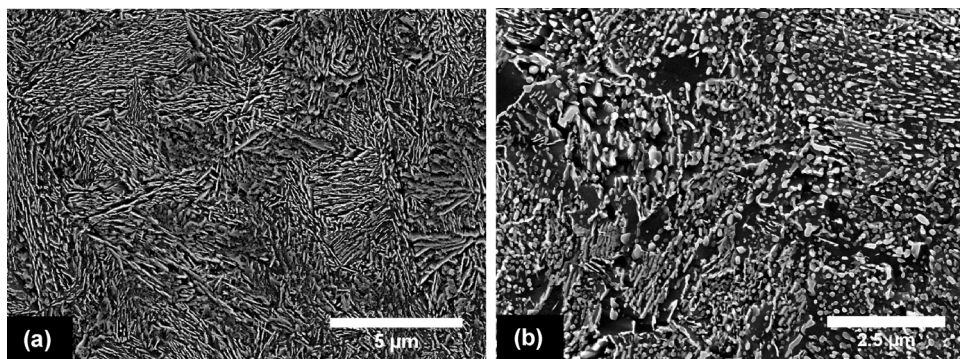

Fig. 13. SEM micrographs showing typical morphology of (a) bainite and pearlite and (b) spheroidite/partial spheroidite.
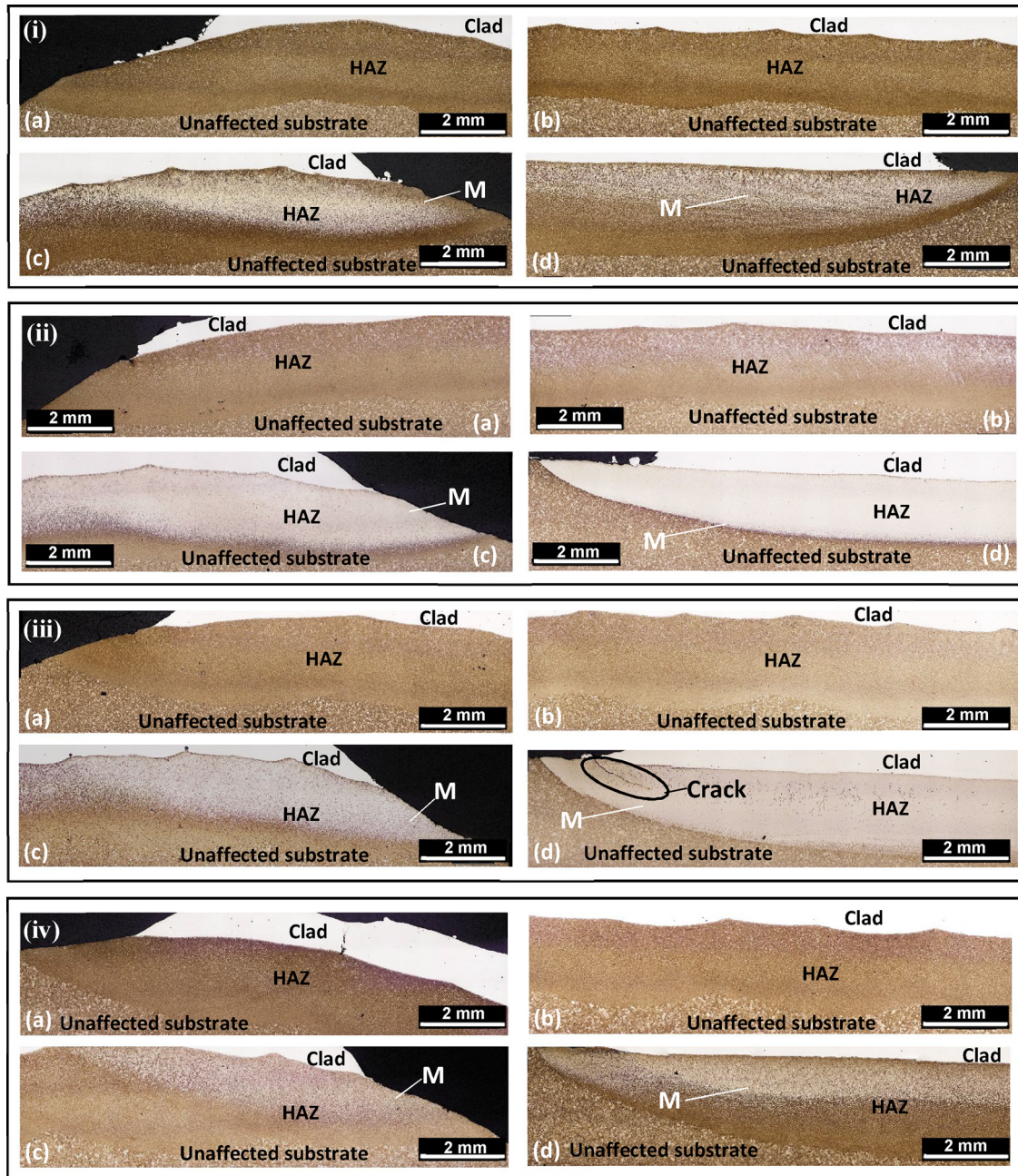
Fig. 14. Heat affected zones and the unaffected substrate of the rail-cross sections at (a) the initial cladding runs - LHS, (b) middle cladding runs, (c) the last cladding runs - RHS, and (d) a typical longitudinal cross-section at the beginning and finishing ends of the cladding runs under (i) 410 L, (ii) 420SS, (iii) Stellite 6 and (iv) Stellite 21 deposits with HTA and single deposition. (M = martensite).

937 ± 8 MPa with typical elastic-plastic behaviour as shown in Fig. 20. Similar measurements for the four depositing materials, also with a 0.6 mm sample thickness, revealed different mechanical behaviour from that of the rail. It can be observed in Fig. 20 that the 420SS, Stellite 6 and Stellite 21 depositing materials exhibited fast brittle fracture, which means minimal plastic deformation was experienced. Fracture forces of 8445 N, 5198 N and 5815 N and their corresponding ultimate shear strength of 1407 ± 29 MPa, 909 ± 19 MPa and 1005 ± 20 MPa were recorded for 420SS, Stellite 6 and Stellite 21, respectively. On the other hand, similar to the rail, elastic-plastic deformation was observed for the 410 L samples, and its failure load and ultimate shear strength were 4550 N and 791 ± 7 MPa, which are 84% of those of the rail.

Investigations of Guduru et al. (2005) and Sellamuthu et al. (2013)

showed a direct relationship between ultimate shear and tensile strength. Thus, a proven estimation of the ultimate tensile strength of 1423 ± 12 MPa can be made for the 410 L deposited layer. Pun et al. (2014) have reported values of ultimate tensile strength being 1384 MPa and 1429 MPa for the nearest equivalent rail grades. It indicates that the 410 L claddings are still within the acceptable range of ultimate tensile strength. All the other depositing materials predicted ultimate tensile strengths values are also well beyond the upper limit of the range.
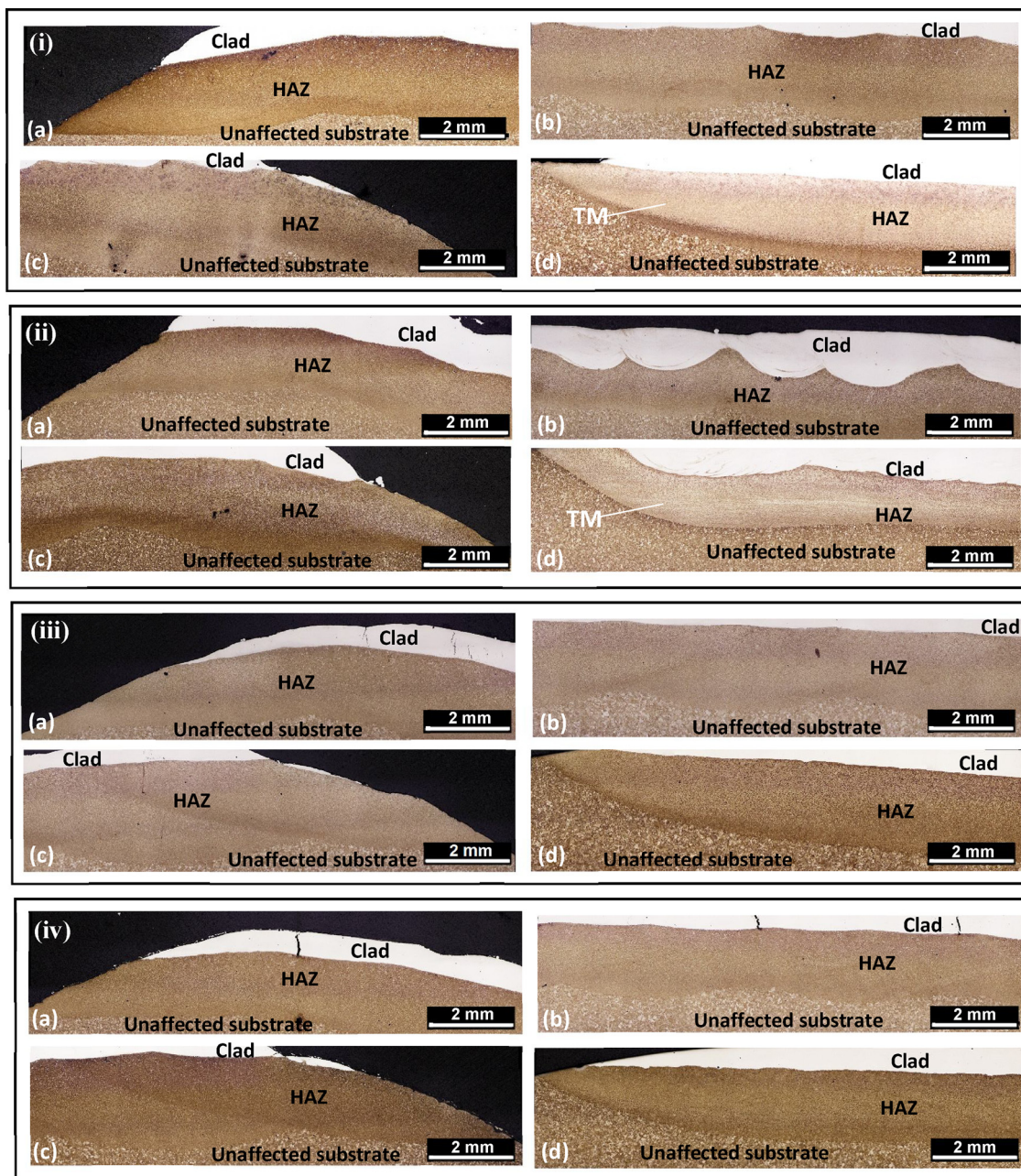
Fig. 15. Heat affected zones and the unaffected substrate of the rail-cross sections at (a) the initial cladding runs - LHS, (b) middle cladding runs, (c) the last cladding runs - RHS, and (d) a typical longitudinal cross-section at the beginning and finishing ends of the cladding runs under (i) 410 L (ii) 420SS, (iii) Stellite 6 and (iv) Stellite 21 deposits with HTB and single deposition. (TM = Tempered martensite).

4. Discussion

4.1. Impacts of cladding materials and processing parameters on cladding quality

A strong metallurgical bond is established between the substrate and the cladding material using laser cladding. As a result, a specific part of the substrate is covered with the superior material. However, it is of great importance to find the appropriate process parameters to achieve required hardness and strength particularly for rail-wheel contact, to reduce the size of the HAZ carbon dilution and to mitigate the tendency to crack.

Owing to the variations in melting points of the cladding materials, evaporation of the molten pool was observed to occur differently between the cladding materials. At a transverse speed of 1000 mm/s and 3

RPM (Group 1), Stellite 6 was susceptible to the heating issue for both single and double deposition, as shown in Fig. 2(c.1) and (c.2). At the transverse speed of 1200 mm/s and 4 RPM (Group 2), 410 L was observed to develop bubbling for the double deposition, as shown in Fig. 3(a.2). The surface of the other cladding materials was observed to be free of defects for the selected ranges of processing parameters. It indicates that each of the cladding materials has its own corresponding optimum processing parameters, which would define the surface quality of the cladding. Therefore, the transverse speed of each cladding material was selected to be the maxima under a condition that resulted in a defect-free surface to minimize the network downtime when conducting the laser treatment. Utilization of Group 1 (1000 mm/min; 3 RPM powder and 3200 W) for 410 L and Group 2 (1200 mm/min; 4 RPM powder and 3200 W) for 420SS, Stellite 6 and Stellite 21 was able to establish deposits with no surface defect.
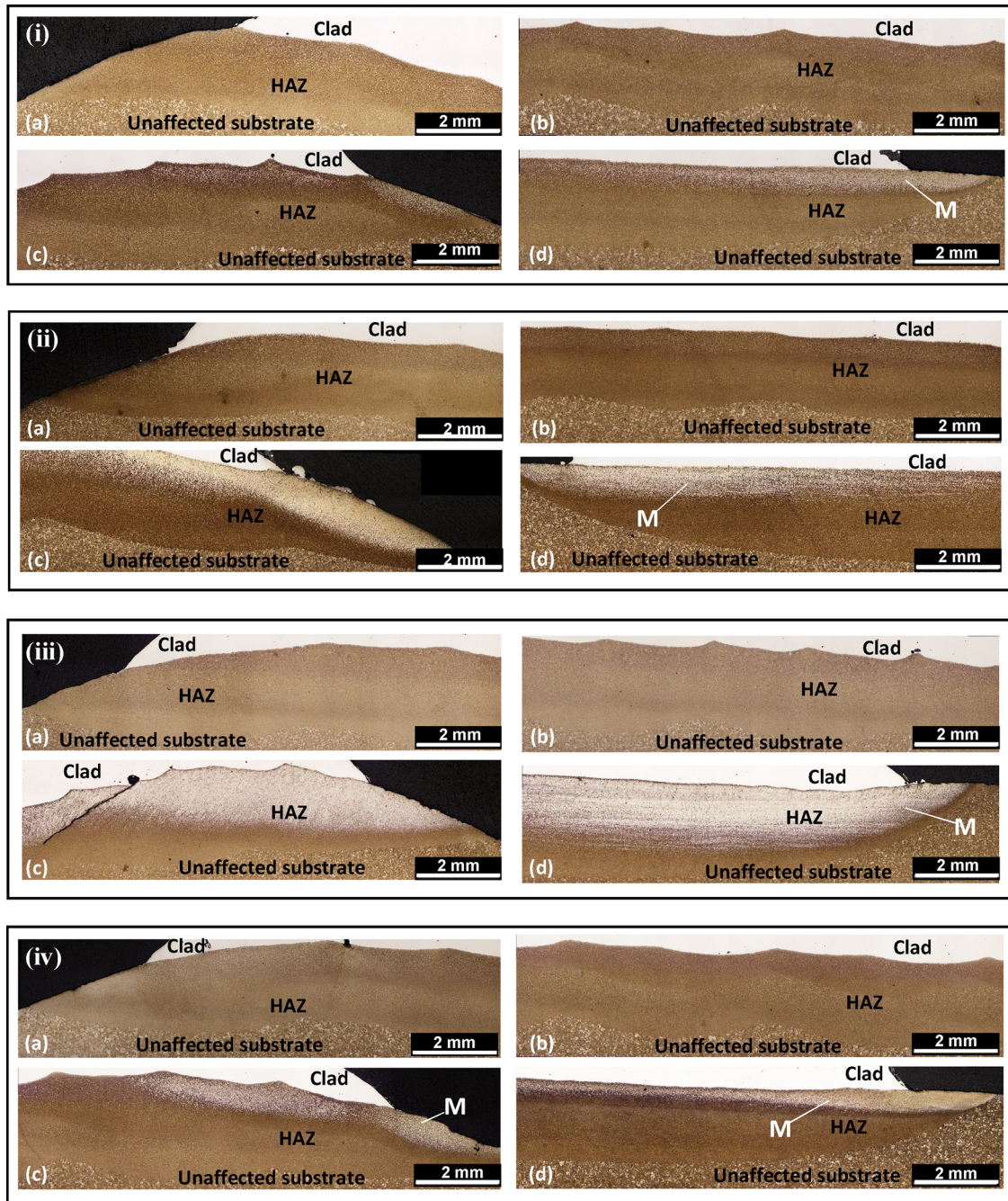
Fig. 16. Heat affected zones and the unaffected substrate of the rail-cross sections at (a) the initial cladding runs - LHS, (b) middle cladding runs, (c) the last cladding runs - RHS, and (d) a typical longitudinal cross-section at the beginning and finishing ends of the cladding runs under (i) 410 L, (ii) 420SS, (iii) Stellite 6 and (iv) Stellite 21 deposits subjected to HTA and double deposition.

4.2. Assessment of structural integrity based on observed microstructural characteristics and measured mechanical properties

Metallurgical analyses were conducted on each of the cladding materials, which were applied under the studied sets of processing parameters, to access their potential structural integrity further. Furthermore, to achieve the hardness within specifications for rail-wheel contact and to prevent/temper any possibility of forming martensite, two groups of specimens were investigated, one of which had been subjected to HTA (preheating only) and other to HTB (preheating, PWHT and slow cooling).

4.2.1. Laser deposited hypereutectoid rails with HTA

For specimen groups subjected to HTA, the deposits were observed to be defect-free. Depending on the chemical composition of the cladding materials, the microstructure of each cladding material was distinctive from one another.

The 410 L deposits were observed with microstructures containing colonies of ferrite and a martensitic matrix, as shown in Fig. 5. Lai et al. (2017a) reported that effects of carbon dilution from the hypereutectoid substrate to the 410 L claddings were severe. In the current work, ferritic microstructure has been noted to occupy the regions near the top surface of claddings for single deposition, and virtually the entire microstructure of the second layers of the double deposition, whereas the remaining portion of the microstructure was the martensite
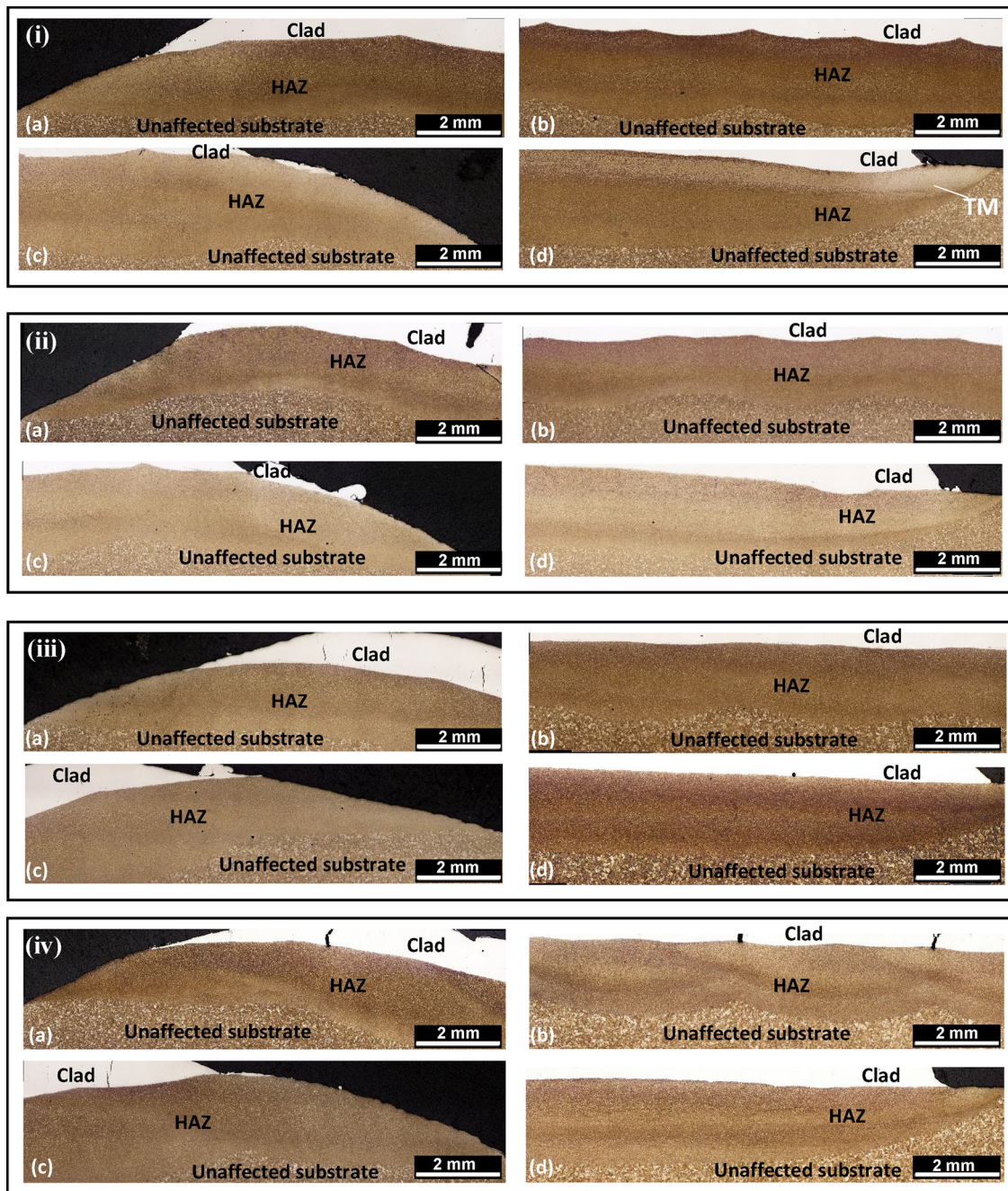
Fig. 17. Heat affected zones and the unaffected substrate of the rail-cross sections at (a) the initial cladding runs - LHS, (b) middle cladding runs, (c) the last cladding runs - RHS, and (d) a typical longitudinal cross-section at the beginning and finishing ends of the cladding runs under (i) 410 L, (ii) 420SS, (iii) Stellite 6 and (iv) Stellite 21 deposits subjected to HTB and double deposition. (TM = Tempered martensite).

matrix. It was attributed to the fact that ferrite contains approximately zero carbon and the carbon dilution from the hypereutectoid substrate was not able to reach such regions with far distances from the cladding-substrate interface. The fast solidification during the cladding process, which provided insufficient time for the alloying elements to homogenize, was also a vital factor in the formation of the ferritic microstructure.

High carbon content in the chemical composition allowed microstructure of 420SS deposits to consist of mainly martensitic dendrites. In the current investigation, not only single deposition of 420SS on the rail substrate was conducted but also double deposition. Microstructural characteristics of (i)–(iii) were found respectively across the thickness of claddings starting from the cladding-substrate

interface for single deposition, as shown in Fig. 6. For double deposition, a similar arrangement of microstructural characteristics was detected in the first layer and the second layer starting from the interface between the two claddings, as shown in Figs. 6 and Fig. 10. This investigation suggests that the microstructural characteristics of the 420SS claddings formed after a rapid solidification was independent on the application of HTA. The absence of HTA in the second deposition, owing to the heat dissipation, did not cause noticeable changes in the microstructural characteristics, which was further confirmed the ineffectiveness of HTA to eliminate martensitic formation from the HAZ.

Consistent with the chemical composition of the Stellite 6, in particular, a high content of Co, a complex combination of interdendritic carbides in a Co-based matrix was observed for the microstructure
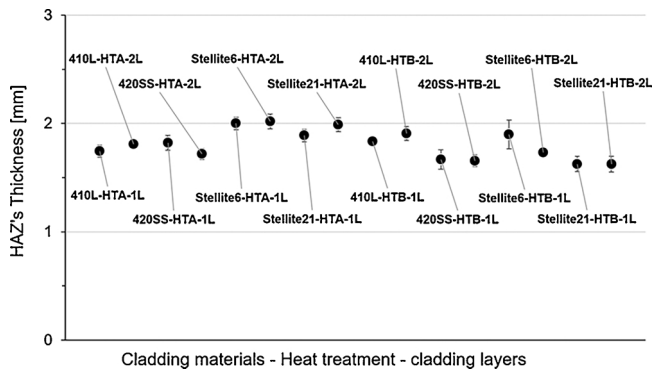
Fig. 18. The heat affected zone (HAZ)'s thickness under the 410 L, 420SS, Stellite 6 and Stellite 21 claddings undergone two separate heat treatments and number of layers.

subjected to HTA, as shown in Fig. 21(a). Dendritic structure of Stellite 6 was fine and homogeneous throughout the deposits. Similar yet finer dendritic morphologies to those of 420SS deposits were also observed, as shown in Fig. 7, which might suggest the occurrence of rapid solidification during the laser deposition. The application of HTA has not modified the microstructural characteristics of the deposits since differences in microstructural characteristics between single and double deposition were minor. The microstructural observations were consistent with the investigation by Gholipour et al. (2011) on laser cladding of 17-4 PH stainless steel with Stellite 6. Moreover, a relatively similar correlation in microstructures between laser treated and other welded processes was revealed, which might be inferred that the laser cladding process has not significantly altered the primary microstructural properties of Stellite 6 alloys while having smaller.

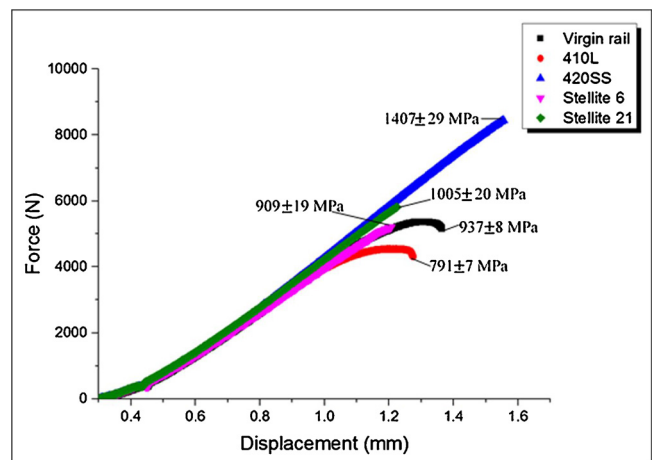An investigation by Davis (2000) reported that, in Stellite 21,

Fig. 20. Force versus displacement results from shear punch tests to determine shear strength values for the 410 L, 420SS, Stellite 6 and Stellite 21 deposited layers subjected to similar heat treatments and processing parameters.

molybdenum (Mo) is employed for solid-solution strengthening instead of tungsten (W), and carbon contents were kept lower than that of Stellite 6 to improve the corrosion resistance of the cladding material. Therefore, microstructures of Stellite 21 deposits were rather distinct from Stellite 6, as shown in Fig. 21. Dendritic structure with the typical dendritic morphologies was also discerned for single and double deposition of Stellite 21 deposits, which also suggests the incapability of HTA in avoiding rapid solidification. Generally, the microstructure consists of Co-base matrix and interdendritic Mo and Cr rich carbides. Cracking, as shown in Fig. 22, was observed for Stellite 21 deposits only at the starting of the second deposition. This might be attributed to the
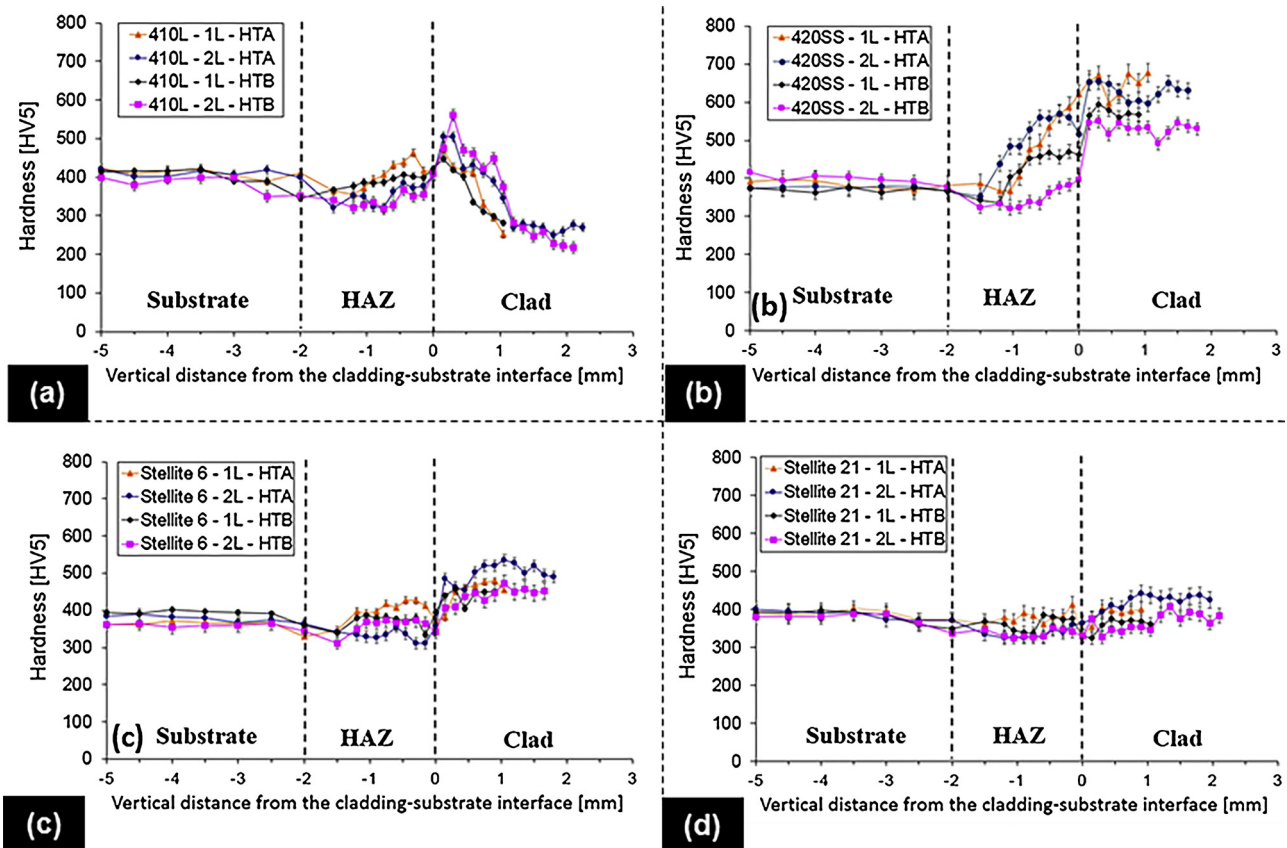

Fig. 19. Distributions of hardness in single (1 L) and double (2 L) deposition of (a) 410 L, (b) 420SS, (c) Stellite 6, (d) Stellite 21 subjected to both HTA and HTB.
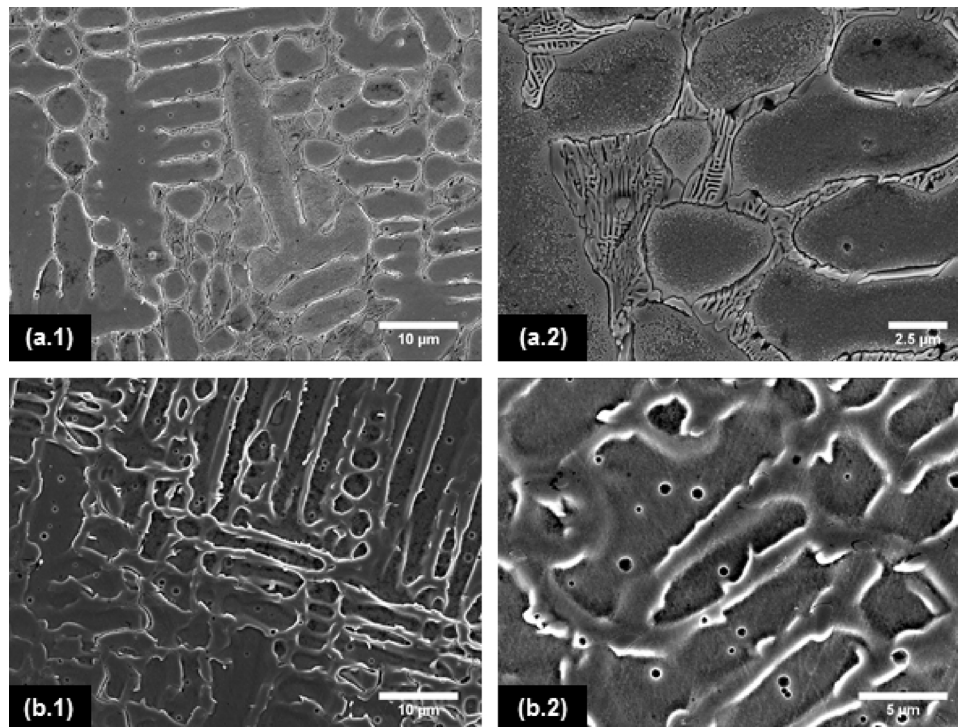
Fig. 21. Scanning electron micrograph of (a) Stellite 6 and (b) Stellite 21's microstructures at (1) low magnification and (2) high magnification.

excessive amount of cumulative heat from HTA, the first and second deposition inputting into the deposits. Given that mechanical properties of Stellite 21 are strongly dependent on the dispersed hard carbides in a CoCrMo alloy, any increase in applied heat input might modify the morphology and distribution of the carbides and facilitate the formation of carbides on the dendritic grain boundaries upon solidification. The carbides on the grain boundaries reduce ductility and, therefore, the sites for crack propagation were observed on the grain boundaries.

Regarding the microstructures of HAZ, irrespective of the cladding materials, martensite was detected in the HAZ due to the inadequacy of the applied preheating regime, as shown in Figs. 14 and 16. The formation of martensite was attributed to the rapid heat dissipation even with a preheating temperature of 350 ℃, through the sizeable enclosing surface area with significantly lower temperature. Cooling rates were therefore rapid enough for the diffusionless transformation to occur and martensite was formed.

4.2.2. Laser cladded hypereutectoid rails with HTB

For specimen groups subjected to HTB, PWHT was employed to alleviate residual stresses, control hardness and improve the strength of

the deposits across the range of cladding materials. Microstructures of 410 L and 420SS were observed with relatively similar characteristics to those with HTA, as shown in Figs. 5 and 6. Nevertheless, severe subsurface cracking occurred for both single and double layers of Stellite 6 and Stellite 21, as shown in Figs. 7 and 8(c) and (d). The overlapping/remelted regions in the microstructures of claddings were the most susceptible regions to cracking. The cracking was determined to be intergranular with typical characteristics of the reheat cracking phenomenon, which commonly happens for the Cr-Mo alloy steels with PWHT. It might be attributed to the combined influence of dilution effects from the high carbon rail substrate, excessive cumulative heat during the laser deposition, creep deformation caused by the relaxation of residual stresses, etc. The occurrence of cracking is unfavourable for utilisation of the cladding process in railway applications. Further investigations are therefore necessary to confirm the cracking mechanisms of the deposits.

Unlike the HAZ of the deposits subjected to HTA, the tempered martensite was observed as a substitute in the HAZ, particularly at the regions near the uncladed surfaces, owing to the influence of PWHT. It suggests that PHWT was effective in tempering the martensite formed
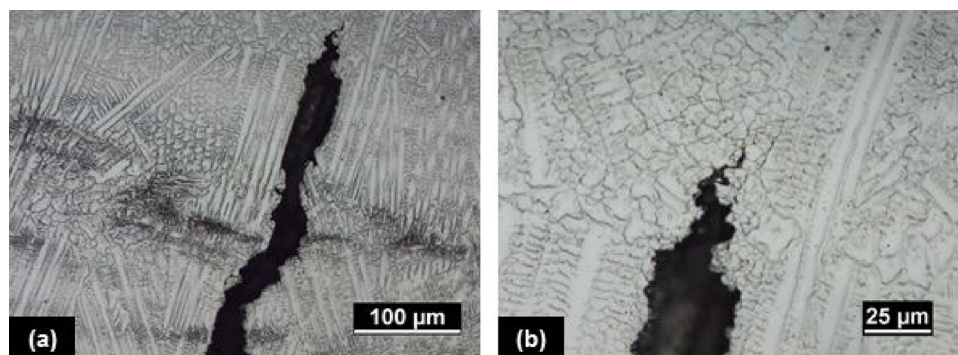

Fig. 22. Scanning electron micrograph of a typical interdendritic crack for Stellite 21 deposits with HTA at the starting of the second deposition. (a) Low magnification, (b) high magnification.

in the HAZ, which was able to mitigate the tendency of cracking in the HAZ. Indeed, no severe cracks were observed, disregarding the variation in cladding materials and cladding layers, as shown in Figs. 15 and 17.

4.3. Assessment of structural integrity based on measured mechanical properties

Investigations by Jin et al. (2011) and Lewis et al. (2015) have shown an inverse relationship between hardness and wear behaviour in wheel-rail contact, i.e. the lower the hardness, the more the wear. Hence, the potential tribological performance of the deposited layers can be estimated using Vickers hardness measurements, provided any microstructural effects are ignored.

When subjected to HTA, 410 L deposits showed the lowest average hardness, i.e. 372–375 HV, among the four considered cladding materials due to its lower carbon content. In contrast, 420SS deposits exhibited the highest values of average hardness, i.e. 629–649 HV which was strongly correlated to the microstructure containing a majority of martensitic dendrites.

Therefore, the hardness values of 420SS deposits were inapplicable for the rail-wheel contact due to the high hardness; the 410 L deposits might be used for cladding as being close to the hardness requirements of 400–500 HV. However, one would need to be aware of the differences in hardness of the deposits compared to those of the parent hypereutectoid rails. If cladding layers were significantly softer or harder than the hypereutectoid parent rail, such that cumulative wear of the cladding layers would respectively be higher or lower than that of the parental rail. It could result in uneven worn surfaces of the cladded rails, which may, in turn, alter the dynamic interaction between wheels and rails, potentially increasing impact loads, and associated noise and vibration. Generally, one would aim for a cladding hardness around 5–10% more or less than the parent rail. Nevertheless, for application as a repair option, the parent rail would be work-hardened already, so the 410 L deposits may not be appropriate for such application. On the other hand, the average hardness values of the Co-base claddings, i.e. Stellite 6 & Stellite 21, fell within the hardness requirements of 400–500 HV. Stellite 6 & Stellite 21 claddings gave an average hardness of 441–452 HV and 390–420 HV, respectively. It suggests a more uniform wear rate could be obtained across the profile of the laser cladded rails, a resulting in wheel-rail contact conditions which were closer to those obtained with the undamaged wheel and rail surfaces. However, for Stellite 21 deposits, cracking was observed at the starting of the second deposition.

For the specimen groups subjected to HTB, the application of PWHT resulted in a reduction in hardness of all the deposits, irrespective of cladding materials. 410 L deposits were observed to experience the smallest reduction, particularly in the second deposition, as shown in Fig. 19 (a). It might be due to the microstructure containing a small portion of martensite and a large volume fraction of ferrite, as shown in Fig. 6. Consequentially, the tempering effects of PWHT on martensitic microstructure were not significant, and a minor reduction in hardness was observed. As the microstructure of 420SS deposits consisted mainly of martensite, the effects of tempering on the microstructure were more discernible. The average hardness of the deposits subjected to HTB reduced nearly 100 HV compared to those subjected to HTA, as shown in Fig. 19(b). Lin and Chen (2006) reported that high hardness of the Co-base deposits originated from the hardness of intermetallic compounds in Co-rich solid solution and hard carbides. In this current work, with the application of PWHT, the average hardness of Stellite 6 and Stellite 21 decreased to comparable values of the parental rail (400 HV), as shown in Fig. 19(a) and (b). The reduction in hardness might be due to the stress relieving effects of the PWHT and presence of the reheat cracks so that the residual stresses were significantly released.

An investigation by Magel (2011) reported that the development of

shear stresses under the contact patch is inevitable in wheel-rail contact conditions, which directly influences the material behaviour, i.e. wear or RCF. Hence, shear punch test data was obtained to assess the relative strength of the rails cladded with the four cladding materials. Only sound and intact deposits were tested. The presented results of the current investigation showed good correlation between the microstructure and the mechanical properties of the cladded rails. By using the 1% offset definition as defined in Karthik et al. (2009)'s work, ultimate shear strength (USS) of 937 ± 8 MPa was established for the unprocessed rail substrate as a reference, as shown in Fig. 20. The USS of 410 L was measured to be 84% of that of the untreated rails, which was also the lowest among the four cladding materials. It might be attributed to the large portion of ferrite in the 410 L microstructure. With the microstructure containing fully martensitic dendrites, the USS value of 420SS was the highest and approximately 500 MPa greater than that of the substrate. The USS of Stellite 6 and Stellite 21 were rather comparable to that of the uncladded rails, which might be derived from the solid-solution strengthening effects of their metal carbides.

As per the above assessments, cladding material of Stellite 6 which was processed using Group 2′s parameters (1200 mm/min; 4 RPM powder and 3200 W) and subjected to HTA was determined to be acceptable. The material was detected with excellent surface and subsurface, it complied with the targeted hardness range between 400 and 500 HV, and the measured ultimate shear strength was comparable to the unprocessed hypereutectoid rail substrate.

5. Conclusions

Influences of applying different laser depositing materials and heat treatment procedures on a hypereutectoid rail steel grade have been investigated. Optimum processing parameters for each of the considered cladding materials have been determined. A suitable cladding material for wheel-rail applications has been selected from the considered premium cladding materials. Two different heat treatment procedures have been performed on the cladding materials using the obtained optimum processing parameters. The main findings can be summarized as follows:

- Defect-free surfaces were established for each of the considered cladding materials by using different combinations of processing parameters. The 410 L claddings were observed to require 1000 mm/min; 3 RPM powder and 3200 W, whereas the 420SS, Stellite 6 and Stellite 21 claddings require the parameter sets of 1200 mm/min; 4 RPM powder and 3200 W to be free from defects.
- Based on the obtained results and considering critical aspects, e.g. surface defects, hardness, material strength, Stellite 6 was recommended to be the most acceptable cladding material for wheel-rail applications out of the considered commonly-used cladding materials.
- The 420SS, Stellite 6 and Stellite 21 claddings showed brittle fracture behaviour in the shear punch test, whereas the 410 L specimens behaved in an elastic-plastic manner similar to the virgin rail.
- Application of preheating only (HTA) was not able to significantly modify the microstructures of all the four cladding materials, whereas a combination of preheating and PWHT (HTB) may cause severe reheating cracks for Co-base alloys, i.e. Stellite 6 and Stellite 21 under the tested parameters. Hence, PWHT must be used with caution for Co-base alloys.
- Irrespective of the number of cladding layers and cladding materials, application of 400-mm long preheating (HTA) was inadequate to prevent the formation of martensite in the HAZ of the cladded rails. The addition of PWHT in HTB can effectively temper the martensite which formed in the HAZ of the cladded rails. Noncracked and consistent HAZ across the entire rail was also achieved.
- The application of preheating only (HTA) and increasing the

number of cladding layers in this study may increase the probability of the martensite formation as a result of the higher rate of cooling. Adding a second cladding layer did not change the thickness of HAZs yet refined the HAZ's microstructure.

Acknowledgements

References

Abioye, T., McCartney, D., Clare, A., 2015. Laser cladding of Inconel 625 wire for corrosion protection. J. Mater. Process. Technol. 217, 232–240.

Aldajah, S., Ajayi, O.O., Fenske, G.R., Kumar, S., 2003. Investigation of top of rail lubrication and laser glazing for improved railroad energy efficiency. J. Tribol. 125, 643–648.

Brandt, M., Sun, S., Alam, N., Bendeich, P., Bishop, A., 2009. Laser cladding repair of turbine blades in power plants: from research to commercialisation. Int. Heat Treat. Surf. Eng. 3, 105–114.

Clare, A., Oyelola, O., Abioye, T., Farayibi, P., 2013. Laser cladding of rail steel with Co-Cr. Surf. Eng. 29, 731–736.

Davis, J.R., 2000. Nickel, Cobalt, and Their Alloys. ASM International.

EN 13674-1, T., 2011. 13674-1: Railway Applications–Track–Rail–Part 1: Vignole Railway Rails 46 kg/m and Above. Brussels.

Farnia, A., Ghaini, F.M., Rao, J., Ocelík, V., De Hosson, J.T.M., 2012. Effect of Ta on the microstructure and hardness of Stellite 6 coating deposited by low power pulse laser treatments. Surf. Coat. Technol. 213, 278–284.

Franklin, F., Weeda, G.-J., Kapoor, A., Hiensch, E., 2005. Rolling contact fatigue and wear behaviour of the Infrastar two-material rail. Wear 258, 1048–1054.

Ganesh, P., Moitra, A., Tiwari, P., Sathyanarayanan, S., Kumar, H., Rai, S., Kaul, R., Paul, C., Prasad, R., Kukreja, L., 2010. Fracture behaviour of laser-clad joint of Stellite 21 on AISI 316L stainless steel. Mater. Sci. Eng. A 527, 3748–3756.

Gholipour, A., Shamanian, M., Ashrafizadeh, F., 2011. Microstructure and wear behavior of stellite 6 cladding on 17-4 PH stainless steel. J. Alloys 509, 4905–4909.

Guduru, R., Darling, K., Kishore, R., Scattergood, R., Koch, C., Murty, K., 2005. Evaluation of mechanical properties using shear–punch testing. Mater. Sci. Eng. A 395, 307–314.

Hankin, G., Toloczko, M., Johnson, K., Khaleel, M., Hamilton, M., Garner, F., Davies, R., Faulkner, R., 2000. An investigation into the origin and nature of the slope and X-axis intercept of the shear punch-tensile yield strength correlation using finite element analysis. Effects of Radiation on Materials: 19th International Symposium.

Harati, E., Malek Ghaini, F., Torkamany, M.J., 2014. Microstructural analysis of laser cladding of stellite 6 on ductile iron. The 6th Swedish Production Symposium. pp. 1–8.

Hemmati, I., Ocelik, V., De Hosson, J.T.M., 2011. Microstructural characterization of AISI 431 martensitic stainless steel laser-deposited coatings. J. Mater. 46, 3405–3414.

Hiensch, M., Larsson, P.-O., Nilsson, O., Levy, D., Kapoor, A., Franklin, F., Nielsen, J., Ringsberg, J.W., Josefson, B.L., 2005. Two-material rail development: field test results regarding rolling contact fatigue and squeal noise behaviour. Wear 258, 964–972.

Jin, Y., Ishida, M., Namura, A., 2011. Experimental simulation and prediction of wear of wheel flange and rail gauge corner. Wear 271, 259–267.

Johnson, K.L., 1987. Contact Mechanics. Cambridge University Press.

Karthik, V., Visweswaran, P., Vijayraghavan, A., Kasiviswanathan, K., Raj, B., 2009. Tensile–shear correlations obtained from shear punch test technique using a modified experimental approach. J. Nucl. Mater. 393, 425–432.

Kou, S., 2003. Welding Metallurgy. John Wiley & Sons.

Lai, Q., Abrahams, R., Yan, W., Qiu, C., Mutton, P., Paradowska, A., Fang, X., Soodi, M., Wu, X., 2017a. Effects of preheating and carbon dilution on material characteristics of laser-cladded hypereutectoid rail steels. Mater. Sci. Eng. A.

Lai, Q., Abrahams, R., Yan, W., Qiu, C., Mutton, P., Paradowska, A., Soodi, M., 2017b. Investigation of a novel functionally graded material for the repair of premium hypereutectoid rails using laser cladding technology. Compos. B Eng. 130, 174–191.

Lewis, S., Lewis, R., Fletcher, D., 2015. Assessment of laser cladding as an option for repairing/enhancing rails. Wear 330, 581–591.

Lin, W., Chen, C., 2006. Characteristics of thin surface layers of cobalt-based alloys deposited by laser cladding. Surf. Coat. Technol. 200, 4557–4563.

Magel, E.E., 2011. Rolling Contact Fatigue: A Comprehensive Review.

Niederhauser, S., Karlsson, B., 2005. Fatigue behaviour of Co–Cr laser cladded steel plates for railway applications. Wear 258, 1156–1164.

Pun, C.L., Kan, Q., Mutton, P.J., Kang, G., Yan, W., 2014. Ratcheting behaviour of high strength rail steels under bi-axial compression–torsion loadings: experiment and simulation. Int. J. Fatigue 66, 138–154.

Rajeev, G., Kamaraj, M., Bakshi, S.R., 2017. Hardfacing of AISI H13 tool steel with stellite 21 alloy using cold metal transfer welding process. Surf. Coat. Technol. 326, 63–71.

Ringsberg, J.W., Skyttebol, A., Josefson, B.L., 2005. Investigation of the rolling contact fatigue resistance of laser cladded twin-disc specimens: FE simulation of laser cladding, grinding and a twin-disc test. Int. J. Fatigue 27, 702–714.

Sellamuthu, P., Collins, P., Hodgson, P., Stanford, N., 2013. Correlation of tensile test properties with those predicted by the shear punch test. Mater. Des. 47, 258–266.

Sexton, L., Lavin, S., Byrne, G., Kennedy, A., 2002. Laser cladding of aerospace materials. J. Mater. Process. Technol. 122, 63–68.

Shariff, S., Pal, T., Padmanabham, G., Joshi, S., 2010. Sliding wear behaviour of laser surface modified pearlitic rail steel. Surf. Eng. 26, 199–208.

Wang, W., Hu, J., Guo, J., Liu, Q., Zhu, M., 2014. Effect of laser cladding on wear and damage behaviour of heavy-haul wheel/rail materials. Wear 311, 130–136.

Xu, G., Kutsuna, M., Liu, Z., Yamada, K., 2006. Comparison between diode laser and TIG cladding of Co-based alloys on the SUS403 stainless steel. Surf. Coat. Technol. 201, 1138–1144.

Zhenda, C., Chew, L.L., Ming, Q., 1996. Laser cladding of WC-Ni composite. J. Mater. Process. Technol. 62, 321–323.